Thermal Conductivity of the Martian Soil at the InSight Landing site from HP^3 Active Heating Experiments

M. Grott[1], T. Spohn[1,2], J. Knollenberg[1], C. Krause[3], T.L. Hudson[4], S. Piqueux[4], N. Mller[1], M. Golombek[4], C. Vrettos[5], E. Marteau[4], S. Nagihara[6], P. Morgan[7], J.P. Murphy[8], M. Siegler[9,10], S.D. King[8], S.E. Smrekar[4], W.B. Banerdt[4]

[1]German Aerospace Center (DLR), Institute of Planetary Research, Berlin, Germany
[2]International Space Science Institute (ISSI), Bern, Switzerland
[3]German Aerospace Center (DLR), MUSC Space Operations and Astronaut Training, Cologne, Germany
[4]Jet Propulsion Laboratory, California Institute of Technology, Pasadena, USA
[5]Department of Civil Engineering, Technical University Kaiserslautern, Germany
[6]Department of Geosciences, Texas Tech University, Lubbock, USA
[7]Colorado Geological Survey, Colorado School of Mines, Golden, USA
[8]Virginia Polytechnic Institute and State University, Blacksburg, USA
[9]Planetary Science Institute, Tucson, AZ, USA
[10]Southern Methodist University, Dallas, TX, USA

Key Points:

- The Heat Flow and Physical Properties Package (HP^3) measured the average thermal conductivity of the martian soil.
- Average soil thermal conductivity in the 0.03 to 0.37 m depth range is 0.039 $\pm$ 0.002 W m^{-1} K^{-1}.
- This implies that 85 to 95% of all particles are smaller than 104-173 μm.

Corresponding author: Matthias Grott, matthias.grott@dlr.de

Abstract

The heat flow and physical properties package (HP^3) of the InSight Mars mission is an instrument package designed to determine the martian planetary heat flow. To this end, the package was designed to emplace sensors into the martian subsurface and measure the thermal conductivity as well as the geothermal gradient in the 0-5 m depth range. After emplacing the probe to a tip depth of 0.37 m, a first reliable measurement of the average soil thermal conductivity in the 0.03 to 0.37 m depth range was performed. Using the HP^3 mole as a modified line heat source, we determined a soil thermal conductivity of 0.039 $\pm$ 0.002 W m^{-1} K^{-1}, consistent with the results of orbital and in-situ thermal inertia measurements. This low thermal conductivity implies that 85 to 95% of all particles are smaller than 104-173 μm and suggests that any cement contributing to soil cohesion cannot significantly increase grain-to-grain contact areas by forming cementing necks, but could be distributed in the form of grain coatings instead. Soil densities compatible with the measurements are 1211^{+149}_{-113} kg m^{-3}, indicating soil porosities of 61 %.

Plain Language Summary

The heat flow and physical properties package (HP^3) of the InSight Mars mission is an instrument package designed to measure the martian planetary heat flow by determining temperature and thermal conductivity in the 0 to 5 m depth range. After inserting the probe to a tip depth of 0.37 m, a first thermal conductivity measurement was performed, and average soil conductivity in the 0.03 to and 0.37 m depth range was found to be 0.039 $\pm$ 0.002 W m^{-1} K^{-1}. Upper limits on soil grain size can be derived from thermal conductivity by a comparison with laboratory measurements under martian atmospheric conditions, and the determined conductivity values indicate that the majority of particles must be smaller than 104-173 μm. The low conductivity further suggests that soil cementation cannot significantly contribute to soil thermal conductivity by forming cementing necks. Rather, any cement is likely distributed in the form of grain coatings, which have little influence on thermal properties. The soil densities compatible with our thermal measurements are 1211^{+149}_{-113} kg m^{-3}, indicating significant soil porosities of about 60%.

1 Introduction

The martian near surface layer consists of sand-sized as well as dust-sized particles (Christensen & Moore, 1992) interspersed with larger rocks, and it's detailed structure depends on the deposition process as well as subsequent surface modifications by eolian and fluvial activity. Under present martian atmospheric conditions sand-sized particles in the 100-600 μm size range can be mobilized by winds (Kok et al., 2012), and dust particles of typical sizes around 2.5 μm are suspended in the atmosphere and can reach the ground in the form of airfall (Pollack et al., 1979), such that aeolian processes are generally recognized to be the prevalent surface modification process on Mars today.

The thermal conductivity is a fundamental physical property of the surface material and determines the rate at which heat can be transferred from the interior to the surface and vice versa. Heat is transported through grain-to-grain contacts, conduction through the pore-filling gas, as well as radiation between individual grains, and the conductivity of the martian soil holds information on the soils bulk porosity, composition, grain size (Presley & Christensen, 1997; Presley & Craddock, 2006; Piqueux & Christensen, 2009a), as well as the state of cementation or induration (Presley et al., 2009; Piqueux & Christensen, 2009b). Thermal properties of the martian soil can thus provide critical information to better understand the local, regional and global geologic processes modifying the surface of Mars, including material redeposition as well as soil-atmosphere interactions. The latter can result in cementation or induration by salts, which may be common on Mars (Mutch et al., 1977; Ditteon, 1982; Moore et al., 1999; Banin et al., 1992; Haskin et al., 2005; Hurowitz et al., 2006) and can have a significant influence on thermal properties by increasing the contact area between individual grains (Piqueux & Christensen, 2009a).

Thermal properties of the martian soil have primarily been estimated from remote sensing infrared observations conducted from orbit (Kieffer et al., 1977; Palluconi & Kieffer, 1981; Mellon et al., 2000; Putzig & Mellon, 2007; Golombek et al., 2008), but some investigations have also been performed on the ground (Fergason et al., 2006; Hamilton et al., 2014; Golombek, Warner, et al., 2020). In general, thermal inertia

$$\Gamma = \sqrt{k\rho c_p} \tag{1}$$

is derived from measurements of the surface brightness temperature, where k is thermal conductivity, ρ is density, and c_p is specific heat capacity. Globally, thermal inertia was

found to have a bimodal distribution (Kieffer et al., 1977; Mellon et al., 2000; Putzig & Mellon, 2007), with peaks around 75 and 250 J m^{-2} K^{-1} $s^{-1/2}$, representing dust covered and dust free surfaces, respectively. Higher thermal inertia units are associated with impact craters and the associated ejecta (Mellon et al., 2000), but it has also been argued that high thermal inertia may be related to soil induration often referred to as duricrust (Jakosky & Christensen, 1986).

Thermal conductivity can be interpreted in terms of soil grain size (e.g., Hamilton et al. (2014)) by a comparison with results from laboratory experiments (Presley & Christensen, 1997; Presley & Craddock, 2006). Estimates of grain size were found to be robust if cementation of the soil is minimal and indurated surface layers are much thinner than the diurnal skin depth. Edwards et al. (2018) compared orbital and rover results with grain size estimates derived from direct microscopic imaging at a dune field in Gale Crater and found that particle sizes derived from the different datasets yield consistent results, indicating that grain sizes of homogeneous material derived from temperature measurements are reliable.

Out of the few measurements from the ground, most have been performed using radiometric methods, and thermal inertia at the Mars Exploration Rover landing sites was determined using the mini-TES instrument for a number of bedforms. Particle sizes derived from these measurements were 45 to 415 μm and were generally found to be consistent with those derived from Microscopic Imager data. Although some discrepancies in the data analysis remained, results indicated that in most cases the relationship between thermal inertia and effective particle size as determined in the laboratory (Presley & Christensen, 1997) also holds for the mini-TES observations (Fergason et al., 2006).

At Gale Crater (4.59°N, 137.44°E) thermal inertia determined using the REMS GTS sensor (Gómez-Elvira et al., 2012) ranged from 265375 J m^{-2} K^{-1} $s^{-1/2}$ along the Curiosity rover's traverse (Hamilton et al., 2014). Furthermore, thermal inertia was found to be 180-215 J m^{-2} K^{-1} at a sand patch called Rocknest. Using thermal inertia as a proxy for grain size and comparing results with those from laboratory experiments (Presley & Christensen, 1997), thermal inertia was found to be generally consistent with particle sizes determined from images (Edgett et al., 2013; Yingst et al., 2013). Millimeter sized particles dominate along the rover's traverse, and thermal inertia at Rocknest indicates particle sizes around 200 μm.

To date, the only direct thermal measurement using needle probes was performed by the thermal and electrical permittivity probe (TECP) during the Phoenix mission, which landed in Vastitas Borealis at 68.22°N 234.25°E and investigated the martian polar regions in a search for subsurface ice (Mellon et al., 2009). TECP measurements indicated a thermal conductivity of 0.085 W m^{-1} K^{-1} and an average ρc_p equal to 1.05· 10^6 J m^{-3} K^{-1} (Zent et al., 2010). The dry material above the ground ice was therefore found to be a good thermal insulator, protecting the ice from large temperature excursions during noontime.

Here we report on direct thermal conductivity measurements at the InSight landing site in Homestead hollow, located in the Elysium Planitia region (4.50°N, 135.62°E) (Banerdt et al., 2020). In the region, the regolith is estimated to constitute a 3-17 m thick layer of broken up material (Warner et al., 2017), and regolith thickness at the landing site itself is estimated to be close to 3 m (Golombek, Kass, et al., 2020). The stratigraphy exposed underneath the InSight lander indicates layering consistent with a surficial dust layer over thin unconsolidated sand, underlain by a cohesive duricrust, which appears to be at least 5-10 cm thick (Golombek, Warner, et al., 2020) and may be underlain by unconsolidated cohesive sand mixed with rocks beneath (Hudson et al., 2020).

Thermal inertia at the landing site was found to be 160 to 230 J m^{-2} K^{-1} $s^{-1/2}$ (Golombek, Warner, et al., 2020), consistent with estimates obtained by the Thermal Emission Spectrometer (TES) (Mellon et al., 2000; Putzig & Mellon, 2007), which determined inertias of ∼200 J m^{-2} K^{-1} $s^{-1/2}$ from orbit. Further, the Thermal Emission Imaging System (THEMIS) of the Mars Odyssey mission shows a high homogeneity of thermal properties at the 100 m scale and a median thermal inertia of around 180 J m^{-2} K^{-1} $s^{-1/2}$ near the landing site (Golombek et al., 2017; Golombek, Kass, et al., 2020), indicating that measurements performed by the InSight radiometer are representative of the regional soil properties. In addition, the lack of significant seasonal variations in thermal inertia suggest the same material extends down to a few tens of centimeters depth.

2 Probe Emplacement

The InSight Mars mission (Banerdt et al., 2020) landed in the Elysium Planitia region on Mars (Golombek et al., 2018; Golombek, Williams, et al., 2020; Golombek, Warner, et al., 2020) on November 26, 2018, and installed a geophysical and meteorological sta-

tion at the landing site. One of InSight's payloads is the Heat Flow and Physical Properties Package (HP^3), which was designed to make the first direct measurement of the martian planetary heat flow (Grott et al., 2007; Spohn et al., 2018; Grott et al., 2019). To determine heat flow, HP^3 is designed to emplace 14 temperature sensors to a target depth of 5 m using a self-hammering penetrator called "the mole". During descent, the depth of the sensors is determined from the attitude of the mole with respect to vertical using static tiltmeters, while simultaneously measuring the amount of paid-out tether. Furthermore, a profile of subsurface thermal conductivity was planned to be determined at 50 cm depth intervals using the mole as a modified line heat source (Hammerschmidt & Sabuga, 2000).

After an initial phase of surface characterization, first the InSight seismometer and then the HP^3 were deployed onto the surface by the lander's robotic arm (Golombek, Williams, et al., 2020). HP^3 then started hammering on Sol 92 of the mission (February 28, 2019), but the depth sensor did not show significant progress despite the fact that 3600 hammering strokes had been executed. Hammering was recommanded at the next opportunity, and an additional 5000 strokes were executed on Sol 94 (March 2, 2019). At this point it became clear that the probe did not penetrate as expected. In an attempt to resolve the anomaly the HP^3 support structure was removed from above the mole, exposing the probe for further investigation on Sol 209 (June 29, 2019).

Insufficient friction to compensate for recoil during hammering was identified as the basic cause of the penetration anomaly (Hudson et al., 2020). Using the lander's robotic arm, friction was provided by first pressing on the side of the mole (Sol 302 to Sol 407; October 2, 2019, to January 18, 2020) and later recoil was compensated by pressing directly onto the back of the mole (Sol 427 to Sol 557; February 8, 2020, to June 20, 2020). In this way, it was possible to bury the back of the mole step-wise to approximately 3 cm below the surface using an additional 1700 strokes in total. The average penetration rate during this time was 0.15 mm per stroke. Together with a mole length of 40 cm and a mole inclination of 30° with respect to vertical, this depth corresponds to a mole tip depth of approximately 37 cm. Therefore, the measurements presented here represent average thermal conductivity in the 0.03 to 0.37 m depth range.

The left hand panel of Fig. 1 shows the configuration of the mole after reaching the maximum depth possible using direct support from the robotic arm to compensate

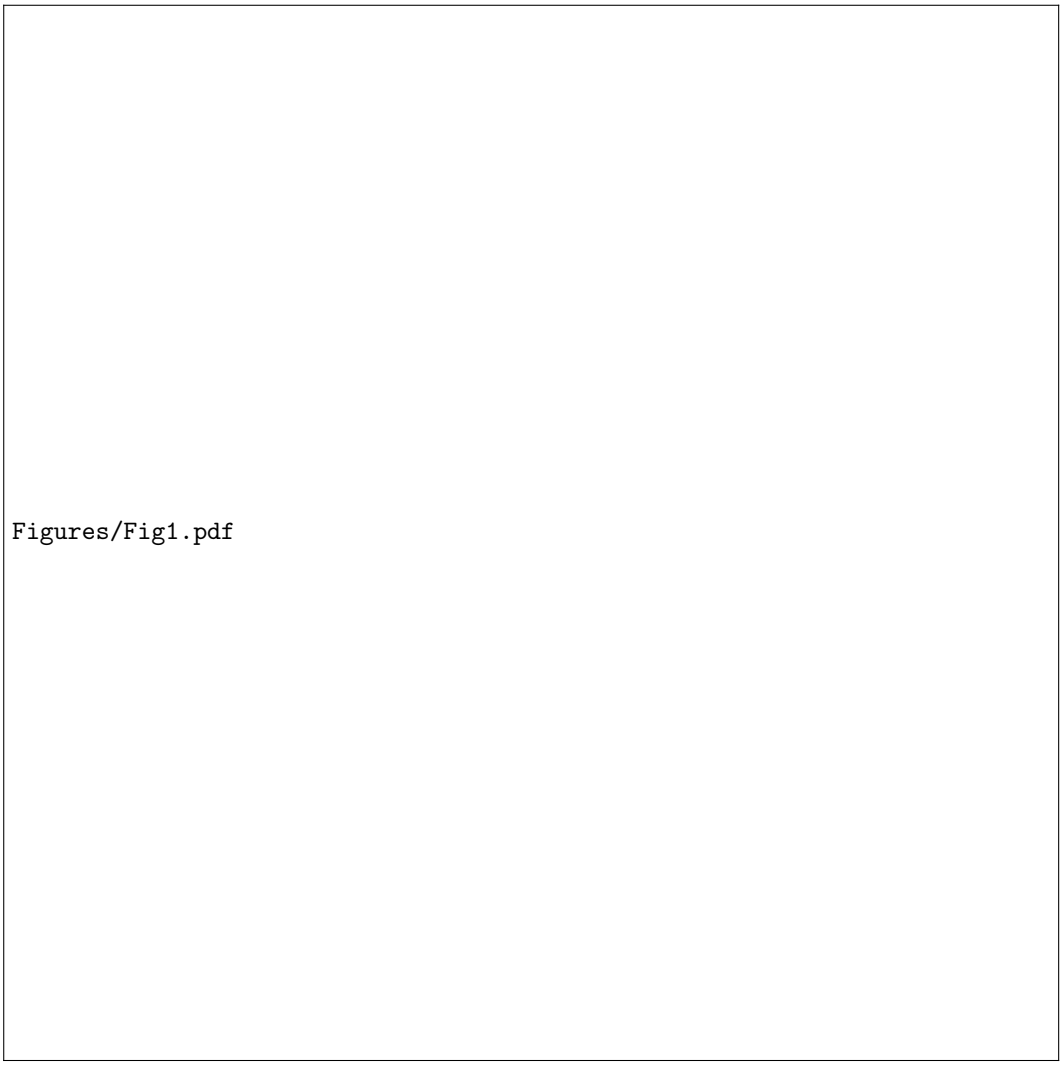

Figure 1. Left: Mole configuration on Sol 598 before scraping soil into the mole pit. Right: Sol 674 after filling the pit and after retracting the robotic arm. The active heating experiment reported here was conducted in this configuration.

recoil. Tilt of the mole as well as a highly cohesive soil layer and a sizeable pit surrounding the mole are apparent. After filling some material into the pit the robotic arm pressed on the mole, but the following hammering attempts between Sol 618 and Sol 645 (August 22 to September 19, 2020) showed no clear indication of significant (>1 cm) further depth progress. Subsequent activities focused on filling the pit to increase friction between the mole and soil, but no additional hammering was performed before the TEM-A measurement on Sol 680.

During the period of mole recovery activities, a number of active heating experiments to determine the thermal conductivity of the soil were performed (Sols 97, 116, 211, 380, and 536). However, all of these suffered from the fact that the mole was not fully buried, thus providing reduced thermal contact to the soil. In addition, direct solar illumination induced a large background temperature variation superimposing the heating curve with a strong diurnal signal and complicating data analysis. In contrast, the mole was fully buried during the measurement conducted on Sol 680, and the corresponding configuration is shown in the right hand panel of Fig. 1. During the measurement, the mole was protected from direct insolation and the residual diurnal temperature amplitude was only 4 K at the effective depth of the temperature sensors in the mole. In the following we report on the results of the Sol 680 measurement and the average soil thermal conductivity in the 0.03 to 0.37 cm depth range.

3 Modeling

3.1 Data Reduction

HP^3 measures thermal conductivity by operating the mole as a modified line heat source (Jaeger, 1956; Hammerschmidt & Sabuga, 2000). During a measurement, a defined amount of heat is provided to the mole's outer hull and the resulting temperature rise is monitored as a function of time (Spohn et al., 2018; Grott et al., 2019). Soil thermal conductivity can then be determined from the rate of self heating, where a fast temperature increase corresponds to low thermal conductivity and vice versa. Note that this method is slightly different from the dual needle technique applied by the TECP probe (Zent et al., 2010), which generates a heat pulse at one needle and measures the temperature rise at a second needle.

Before the active heating experiment was started on Sol 681, the background temperature drift was monitored for 2 Sols. Operations were then timed such that heating started at 21:00 local true solar time (LTST), thus allowing temperature perturbations induced by direct insolation to decay, while at the same time maximizing the time before sunrise. Furthermore, care was taken to ensure that sources of shadow like the robotic arm did not move during the experiment to minimize day-to-day temperature variations. The heating power of the probe was set to 2 W to increase the temperature rise during the heating phase to the greatest possible amount, thereby increasing the signal to noise ratio with respect to background temperature variations.

Temperature data obtained for the active heating experiment conducted between Sols 680 and 682 are shown in Fig. 2(a), where temperature is given as a function of LTST and color-code indicates the Sol of the measurement. The heating power dissipated in the probe is shown in panel (b) of the figure for the same time frame, demonstrating that heating power was kept constant by the control loops in the HP^3 electronics during the experiment. As shown, temperature was monitored on Sol 680 and Sol 681 before switching on the heaters at 21:00 LTST on Sol 681. The background temperatures show a diurnal amplitude of 4 K, with maximum temperatures reached at 16:40 and minimum temperatures at 8:00 LTST. As is evident from the figure, background temperatures are highly repeatable, and we found day-to-day variations to be smaller than 80 mK.

We then extracted the heating curve between Sol 681 21:00 LTST and Sol 682 21:00 LTST by subtracting the background temperatures from Sol 680 21:00 LTST to Sol 681 21:00 LTST from the data, and temperatures were then referenced to the start of the heating interval at 21:00 LTST on Sol 681 to obtain the temperature rise ΔT as a function of time, which is shown in Fig. 2(c). Furthermore, data was downsampled from 5548 to 1000 points by linear interpolation to save computing time. A slight change of slope caused by background temperature fluctuations is visible during the final hours of heating, and we disregard data at times later than 21 h 40 min after start of heating for the data inversion below. Furthermore, data before 1 h was also not considered, as this part of the heating curve is most sensitive to the unknown contact conductance between probe and soil. Therefore, to reduce uncertainties associated with the unknown contact, we performed inversions between 1 h and 21 h 40 min only. Fig. 2(d) shows the logarithmic time derivative of the heating curve to illustrate the amount of scatter, which is caused by short-term temperature fluctuations resulting from the diurnal temperature forcing.

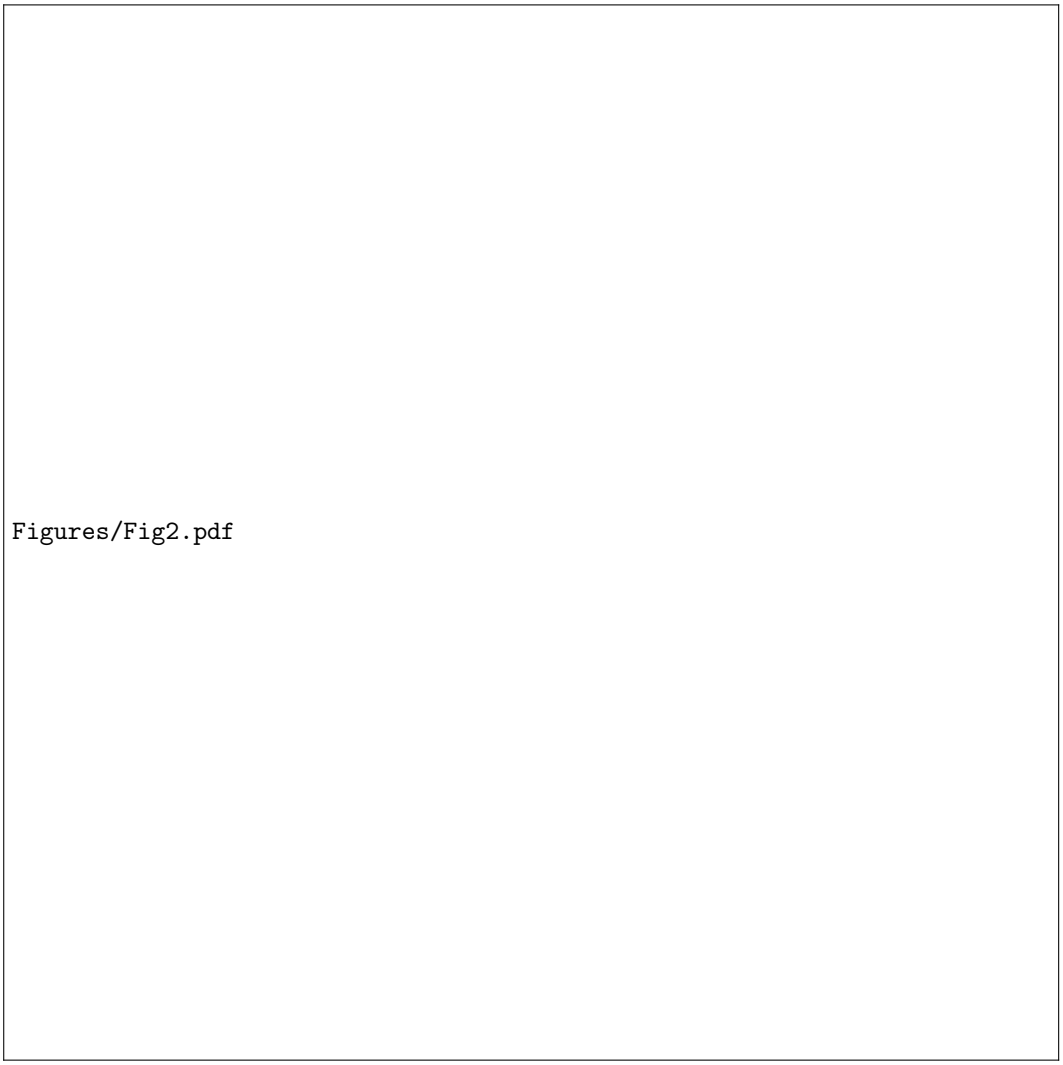

Figure 2. Illustration of steps taken during data reduction. (a) Temperature as a function of local true solar time (LTST) for the three Sols of the experiment. Heating was activated on Sol 681 at 21:00 LTST and continued for 24 h. (b) Heating power as a function of local time for the same time frame. (c) Heating curve (temperature rise as a function of time) extracted from the data shown in (a) (see text for details). (d) Logarithmic time derivative of the temperature rise shown in (c) as a function of time.

Therefore, rather than using the logarithmic time derivative as a fitting function (Spohn et al., 2018; Grott et al., 2019), we use the heating curve itself to determine soil thermal conductivity in the following.

3.2 Data Inversion

We used forward modeling of the heating curve to determine the admissible range of soil parameters. The temperature response to heating of the mole was modeled using a finite element model in cylindrical geometry. The model encompasses a reduced thermal model of the mole including the hull, motor, hammering mechanism, heaters, the science tether connecting the mole to the electronics, and the surrounding soil. The model solves the initial value problem posed by the heat conduction equation and associated boundary conditions starting from thermal equilibrium, and thermophysical properties of the mole and soil need to be prescribed. In addition, thermal contact conductance between the mole and soil is explicitly taken into account, as this can have a significant influence on the temperature rise during the first part of the experiment (also compare Grott et al. (2010) for the lunar case). Details of the finite element model are given in Grott et al. (2019).

To determine the range of admissible soil parameters, we ran Monte-Carlo simulations varying soil thermal conductivity k, soil density ρ, as well as thermal contact conductance between probe and soil H to determine parameter combinations which allowed us to fit the heating curve within admissible limits. The latter were defined based on the observation that background temperature drift was reproducible to within 80 mK on consecutive sols. Furthermore, probe calibration may have drifted as a consequence of being exposed to diurnal temperature cycles. Temperature drift can result in an additional 0.4% uncertainty for temperature difference measurements (Grott et al., 2019), and given a temperature rise of 37.3 K during the measurement, potential sensor drift adds an additional uncertainty of 150 mK. Assuming Gaussian uncertainty propagation, total admissible uncertainty δT is then given by

$$\delta T = \sqrt{\delta T_{var}^2 + \delta T_{drift}^2} \tag{2}$$

where δT_{var} and δT_{drift} are the uncertainty contributions stemming from day to day variations and potential sensor drift, respectively. Therefore, we require the forward model to reproduce temperatures to within $\delta T = 170$ mK.

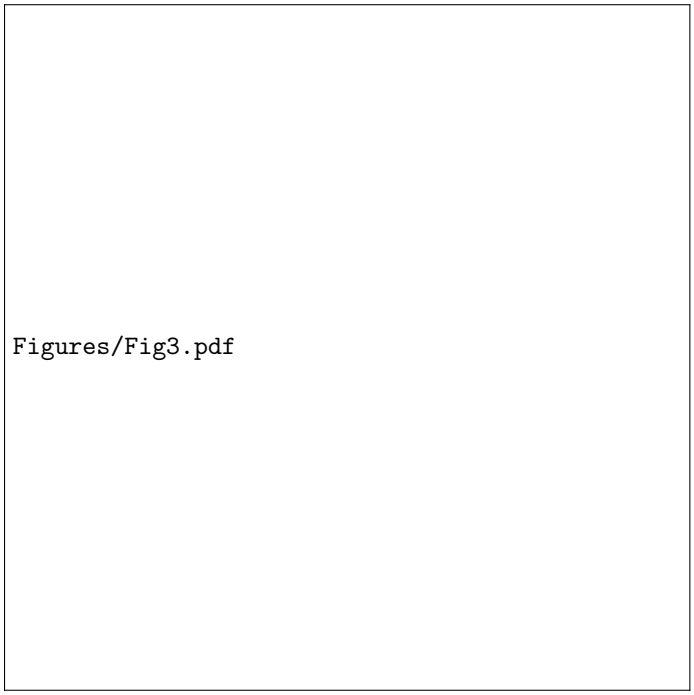

Figure 3. Illustration of the temperature distribution in the finite element model at the end of the heating period. The soil thermal conductivity used in the model was 0.04 W m^{-1} K^{-1}, heating power was 2 W, the back of the mole was assumed to be 3 cm below the surface.

For each model run of the Monte-Carlo simulation, the modeled temperature $T_{mod}(t, k, \rho, H)$ was then compared to the measured temperature rise $T_{dat}(t)$ and the root mean square deviation between the two quantities was determined according to

$$\Delta T_{rms}(k, \rho, H) = \left(\sum_{i=1}^{n} (T_{mod}(t_i, k, \rho, H) - T_{dat}(t_i))^2 / n \right)^{\frac{1}{2}} \quad (3)$$

Here, $n = 1000$ is the number of measurement points, and $t_1 = 1$ h and $t_n = 21$ h 40 min correspond to the beginning and the end of the inversion interval, respectively (see above). In case $\Delta T_{rms}(k, \rho, H) < \delta T$, the combination of parameters k, ρ, and H was considered admissible

An illustration of the results of the finite element model is shown in Fig. 3, where the color coded temperature field is shown for the best fitting model. Heating was active for 21 h 40 min at a heating power of 2 W, and soil thermal conductivity was assumed to be 0.039 W m^{-1} K^{-1}. Although heat transport is primarily in the radial direction, some heat is also lost along the mole axis, illustrating the need to consider a probe with finite length in contrast to analytical solutions for this type of heat conduction prob-

lem (Jaeger, 1956). The computational domain has a diameter of 0.4 m, large enough to minimize boundary effects, and the heat from the mole penetrates a few centimeters into the soil.

An additional constraint that can be considered to restrict the range of admissible models is posed by the surface thermal inertia, which is sensitive to the upper ∼0.07 m of the soil and ranges from 160 to 230 J m^{-2} K^{-1} s$^{-1/2}$ at the landing site (Golombek, Warner, et al., 2020). If soil parameters are assumed to be constant as a function of depth, parameter combinations determined here should also satisfy this additional constraint. Here we assume a soil heat capacity c_p of 630 J kg^{-1} K^{-1} (Morgan et al., 2018) to convert density and thermal conductivity into thermal inertia Γ, and models satisfying the additional constraint $160 \leq \Gamma \leq 230$ J m^{-2} K^{-1} s$^{-1/2}$ (Golombek, Warner, et al., 2020; Piqueux et al., 2021) will be discussed in addition to the models fitting the heating curve only.

4 Results

4.1 Monte Carlo Simulations

We calculated forward models of the heating experiment varying the soil thermal conductivity k, density ρ, as well as the thermal contact conductance between probe and soil H, searching for models which fit measured temperatures within error bounds and within the constraints posed by the surface thermal inertia. To reduce the number of Monte-Carlo simulations, we first conducted a series of test calculations, varying thermal conductivity between $0.01 \leq k \leq 0.1$ W m^{-1} K^{-1}, soil density between $600 \leq \rho \leq 1800$ kg m^{-3}, and contact conductance between $3 \leq H \leq 250$ W m^{-2} K^{-1} to narrow down the parameter space. We found that only conductivities between 0.034 and 0.045 W m^{-1} K^{-1} yielded admissible models, such that the full Monte-Carlo run was restricted to these conductivities in the following. In total, 45000 models were calculated and parameters were assumed to be equally distributed in the above intervals. For each draw of parameters, the resulting model was compared with the data and 229 models reproduced measured temperatures within errorbounds. Out of these models, 102 satisfied the additional constraint posed by the surface thermal inertia.

Results of the calculations are shown in Fig. 4, where the best fit model is shown together with the data and associated uncertainties in panel (a). As is evident, the model

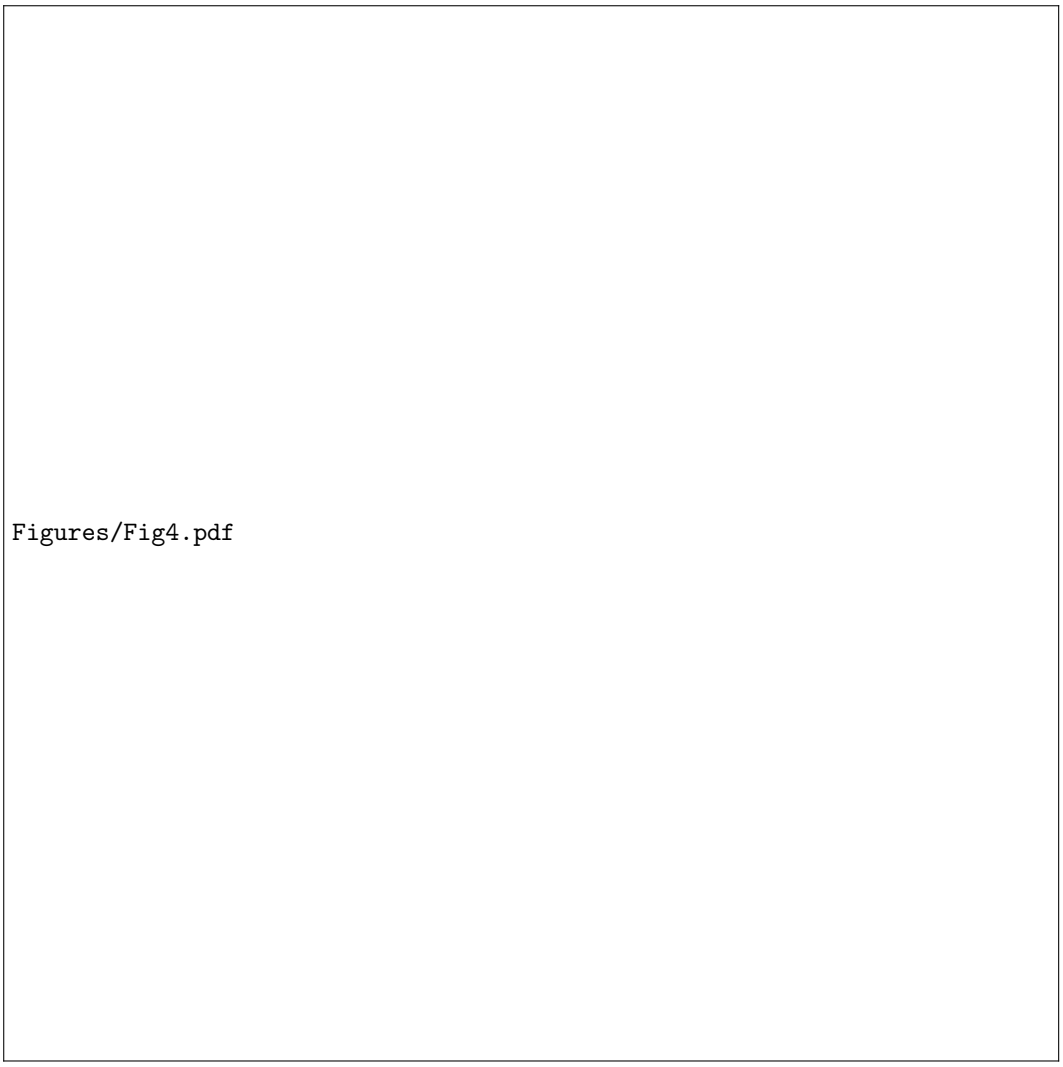

Figure 4. Result of the Monte-Carlo inversion. (a): Temperature rise as a function of time (black) together with the associated measurement uncertainty (gray) during the Sol 680-682 active heating experiment together with the best fit model (red). (b) Logarithmic time derivative of the temperature rise as a function of time (black) together with the best fit model (red). (c) Histogram of thermal conductivities for the models fitting the prescribed uncertainty within error bounds (1-σ, green) as well as histogram of models also fitting the constraint posed by the surface thermal inertia (TI, red). (d) Same as (c), but showing the histogram of admissible soil densities.

fits the data excellently, and the residual root mean square misfit is only 60 mK. The logarithmic time derivative of the data is shown together with the best fit model in panel (b), demonstrating that the model also fits the time derivative well on average. Histograms of admissible thermal conductivities are shown in Fig. 4(c), where the histogram for models fitting the heating curve is shown in green (1-σ), while models satisfying the additional constrain posed by the observed surface thermal inertia are shown in red. For the two cases considered, thermal conductivity is $k = 0.0395 \pm 0.0006$ and $k = 0.0395 \pm 0.0008$ W m^{-1} K^{-1}, respectively. Overall, only a very small range of thermal conductivities fits the data, allowing us to put tight constraints on the admissible values.

Histograms for the admissible soil density are shown in Fig. 4(d), and a large spread is visible in the range of admissible values. The Median density for models satisfying the heating curve constraint is 1007 kg m^{-3} and the 25th and 75th percentile are given by 993 and 1184 kg m^{-3}, respectively, corresponding to an interquartile range or midspread of 191 kg m^{-3}. For models satisfying the additional constraint posed by the surface thermal inertia, the median density is 1211 kg m^{-3} with 25th and 75th percentiles of 1098 and 1360 kg m^{-3}, corresponding to a midspread of 262 kg m^{-3}. Finally, contact conductances compatible with the available constrains have median contact conductances of 70 and 28 W m^{-2} K^{-1} for models satisfying the heating curve and the thermal inertia constraint, respectively (not shown). The 25th and 75th percentiles are 30 and 121 W m^{-2} K^{-1} as well as 19 and 37 W m^{-2} K^{-1}, respectively. For comparison, 10 W m^{-2} K^{-1} corresponds to the conductance across a 1 mm wide, CO_2 filled gap, whereas 2 W m^{-2} K^{-1} would correspond to purely radiative coupling at 220 K. Therefore, contact conductances needed to fit the data are reasonable.

4.2 Uncertainty Error Budget

The total measurement uncertainty for the determination of thermal conductivity from HP^3 active heating experiments was estimated by Grott et al. (2019) and found to be 3.7 %. However, it was assumed that the influence of the unknown soil density and contact conductance would be small due to the fact that the logarithmic time derivative of the temperature rise at large times t could be used for the fitting. As this is not the case for the dataset considered here, the contributions of unknown soil density and contact conductance to the uncertainty budget need to be reassessed.

Error Source	Value [%]	Distr.	σ [%]	Remarks
Sensor Heat input	0.1	normal	0.1	Grott et al. (2019)
Soil density, thermal contact	2	normal	2	This paper
Modeling	4	uniform	2.3	Grott et al. (2019)
Reference method	2.5	normal	2.5	Grott et al. (2019)
Total 1σ Uncertainty			3.9	

Table 1. Error sources taken into account for determining the thermal conductivity uncertainty budget. Uncertainty, distribution function, as well as error contribution σ are given together with an indication of how the individual contributions were derived. Following the relevant standards (VIM, 2004; GUM, 2008), uniformly distributed uncertainties propagate into the total error budget weighted by one over the square root of three. Stated uncertainties are 1σ confidence limits.

Total measurement uncertainty for the determined thermal conductivity σ_k is given by Gaussian error propagation, and

$$\sigma_k = \left(\sigma_Q^2 + \sigma_{reg}^2 + \sigma_{mod}^2 + \sigma_{THS}^2\right)^{1/2} \tag{4}$$

Here, σ_Q is the uncertainty associated with determining the heat input into the TEM-A foils, σ_{reg} is the contribution stemming from the allowable spread of models determined using the Monte-Carlo simulations above, and σ_{mod} is the uncertainty associated with the imperfections of the finite element model representing the mole. The latter has been estimated during instrument calibration by a comparison with measurements in a low thermal conductivity granulate (Grott et al., 2019). Finally, σ_{THS} is the uncertainty of the reference measurement originally used to calibrate the finite element model (Hammerschmidt & Sabuga, 2000). The numerical values of these contributions are summarized in Table 1, and a total 1-σ uncertainty of 3.9 % is obtained for the conductivity determined here. Given a best fit thermal conductivity of 0.039 W m^{-1} K^{-1}, this corresponds to an uncertainty of $\pm$0.002 W m^{-1} K^{-1}.

4.3 Particle Size

Thermal conductivity determined from the active heating experiment can be interpreted in terms of soil grain size (e.g., Fergason et al. (2006)) by a direct comparison with laboratory measurements under martian atmospheric conditions (Presley & Christensen, 1997; Presley & Craddock, 2006), and such estimates have been shown to be robust if the material is homogeneous and any indurated surface layers are much thinner than the diurnal skin depth (Edwards et al., 2018). Given soil thermal conductivity k in units of [W m^{-1} K^{-1}], particle diameter d in units of [μm] can be estimated from

$$d = \left(\frac{k}{CP^{0.6}} \right)^{-1/(0.11 \log(P/K))} \tag{5}$$

where P is atmospheric pressure in torr, and $C = 0.0015$ and $K = 8.1 \cdot 10^4$ are empirical fitting constants (Presley & Christensen, 1997). Eq. 5 is valid for thermal conductivities less than 0.1 m^{-1} K^{-1}, while larger conductivities are more difficult to interpret. Presley & Craddock (2006) have shown that the thermal conductivity of soils which include a variety of particle sizes is dominated by the largest grains, and Eq. 5 should provide a reasonable estimate of the size for which 85 to 95% of the particles are smaller than the size determined using the above equation. A thermal conductivity-derived particle size is therefore closer to a maximum particle size, rather than an average or modal size. Errors in deriving particle sizes with this method are expected to be less than 1015% (Presley & Christensen, 1997), provided cementation does not play a significant role.

Results of applying Eq. 5 to the thermal conductivity range of 0.01 to 0.05 W m^{-1} K^{-1} (corresponding to thermal inertias of 100 to 240 J m^{-2} K^{-1} s$^{-1/2}$ assuming $\rho c_p = 10^6$ J m^{-3} K^{-1}, Neugebauer et al. (1971)) are shown in Fig. 5, where particle diameter is shown as a function of thermal conductivity (solid line) together with a 15% uncertainty interval (gray). Grain sizes corresponding to a thermal conductivity of 0.039 $\pm$ 0.002 W m^{-1} K^{-1} are 136^{+37}_{-32} μm, corresponding to very fine to fine cohesionless sand.

Images taken by the InSight Instrument Deployment Camera (IDC, Maki et al. (2018)) show that steep walls can be supported by the soil at the landing site. This indicates that the assumption of cohesionless sand may be an oversimplification. Rather, soil properties appear to be similar to those at the Phoenix landing site, for which trenches scraped by the robotic arm's scoop exhibited steep walls (Mellon et al., 2009). Overall, cohesion at the InSight landing site is estimated to be at least 1-1.9 kPa (Golombek, Warner, et al., 2020), but may be as high as 14.5 kPa (Marteau et al., 2021), and the influence of

Figure 5. Particle diameter as a function of soil thermal conductivity according to the model of Presley & Christensen (1997) (black). The estimated 15% particle size uncertainty of the model is indicated in shades. The grain size derived from the thermal conductivity determined here is indicated in red, while the grain size derived assuming 0.02 vol% of cement forming necks between particles is indicated in yellow. For reference, the thermal inertia corresponding to the considered thermal conductivities assuming $\rho c_p = 10^6$ J m^{-3} K^{-1} (Neugebauer et al., 1971) is also given.

cementation by, e.g., clays, carbonates, and chloride bearing minerals and salts (see Piqueux & Christensen (2009b) and references therein) should also be considered.

Depending on the distribution of cementing agents, already tiny amounts of cement can increase inter-grain contact and thus thermal conductivity. Assuming cement to primarily form pendular rings at necks between grains, already 0.02 vol% of cement would increase thermal conductivity by a factor of two according to the model of Piqueux & Christensen (2009b). Using Eq. 5, this reduction in the underlying conductivity from values of around 0.04 W m^{-1} K^{-1} to 0.02 W m^{-1} K^{-1} would correspond to grain sizes of 30^{+8}_{-7} μm (see Fig. 5). Therefore, lightly cemented dust-sized particles would also be consistent with the thermal properties determined here.

5 Summary and Discussion

The heat flow and physical properties package (HP^3) of the InSight Mars mission has conducted direct thermal conductivity measurements of martian soil. After initial problems with inserting the probe into the soil, the mole was fully buried and a tip depth of 0.37 m was reached. The active heating experiment was carried out on Sols 680 to 682 of the mission, and average thermal conductivity in the 0.03 to 0.37 m depth range was found to be 0.039±0.002 W m^{-1} K^{-1}. In addition, median soil density was constrained to values of 1007^{+176}_{-74} kg m^{-3} using Monte-Carlo simulations. Assuming that soil density, heat capacity, and thermal conductivity in the investigated depth range are similar to those in the upper few centimeters of the soil, the range of admissible thermal inertia determined by Golombek, Warner, et al. (2020) further constrains the soil density to a median value of 1211^{+149}_{-113} kg m^{-1}.

The numerical model employed to determine thermal conductivity uses cylindrical symmetry, while the mole was inclined at an angle of 30° with respect to vertical. Therefore, a 3-dimensional model would in principle be needed, but since the distance probed by the heat pulse is only a few centimeters (compare Fig. 3), the surroundings of the mole can be assumed to be homogeneous to a good approximation. Therefore, the influence of deviations from the ideal cylindrical symmetry is considered to be small.

As is evident from the history of probe emplacement (Sec. 2), some caution is needed when interpreting the results, as the mechanical configuration of part of the sampled soil may have been perturbed in the emplacement process (also see Marshall et al. (2017)).

Soil around the mole is likely compacted to an unknown degree, such that strictly speaking the thermal conductivity values reported here need to be considered as upper limits. One method to quantify the influence of compaction would be to independently estimate thermal diffusivity from the amplitude of the diurnal temperature wave measured at the mole, but such an analysis is beyond the scope of this paper.

Thermal conductivity of the soil is expected to be temperature dependent (Morgan et al., 2018). Therefore, it would have been preferable to use less heating power and stimulate a smaller temperature response during the experiment, but this needed to be balanced against the desire to obtain a good signal to noise compared to the background temperature fluctuations. Therefore, it was decided to run the experiment using a heating power of 2 W, inducing a temperature rise of 37.3 K. This may have increased the measured thermal conductivity by up to 8 % as compare to a measurement at the background temperature (Morgan et al., 2018).

Thermal conductivity values determined here are more than a factor of two smaller than those determined with the TECP instrument on the Phoenix Mars mission (Zent et al., 2010), for which a thermal conductivity of 0.085 W m^{-1} K^{-1} was determined for the upper few centimeters of the soil. This may not be surprising given the presence of near surface ground ice as well as the abundant presence of cementing agents like perchlorate salts at the polar Phoenix landing site (Hecht et al., 2009; Kounaves et al., 2014). However, overall even 0.085 W m^{-1} K^{-1} is relatively small, and both values indicate that the martian soil is a good thermal insulator. Furthermore, both values fall within the expected conductivity range for uncemented martian soils, which is 0.02 to 0.1 W m^{-1} K^{-1} (Grott et al., 2007).

As discussed in Sec. 4.3, the presence of cement can have a large influence on thermal conductivity. If present in the form of cementing necks, increased grain-to-grain contact areas will significantly increase thermal conductivity (Piqueux & Christensen, 2009b), and already 0.02 vol% of cement would increase thermal conductivity by a factor of two. As discussed, this would imply dust sized particles to be present. However, such small particle sizes seem to be implausible, as Homestead hollow appears to be filled by eolian deposits (Grant et al., 2020; Weitz et al., 2020) and the saltation limit for particles that can be mobilized by winds is 100 to 600 μm (Kok et al., 2012). Therefore, it seems more likely that cement present in the soil acts to increase cohesion but has only a small

influence on grain-to-grain contact areas. This could for example be the case if cement is distributed in the form of grain coatings rather than cementing necks (Piqueux & Christensen, 2009b). In this case, thermal conductivity would increase linearly as a function of volumetric cement content (Martinez, Alejandro et al., 2020) rather than the very steep increase expected for deposition at particle contacts only (Piqueux & Christensen, 2009b).

Whether cement deposition in the form of particle coatings is sufficient to provide the soil cohesion necessary to create clods and to support steep walls remains to be investigated. At the InSight landing site, cohesion of at least 1-1.9 kPa is required (Golombek, Warner, et al., 2020), but may be as high as 14 kPa (Marteau et al., 2021). Lower bounds on cohesion are similar to values found for crusty to cloddy soil at other landing sites (0-4 kPa), whereas upper limits are similiar to cohesion estimates for blocky, indurated soil (3-11 kPa, see Golombek et al. (2008), Herkenhoff et al. (2008) and references therein). Cohesion values determined at Insight are comparable to or higher than the 0.2 ± 0.4kPa to 1.2 ± 1.8 kPa derived from trenching experiments at the Phoenix landing site (Shaw et al., 2009). Considering that perchlorate is present at a level of 0.6 wt% at the Phoenix site (Hecht et al., 2009; Kounaves et al., 2014), similar amounts of cement could be present at InSight. However, these would need to be distributed in the form of particle coatings to be compatible with the thermal constraints discussed above.

The underlying particle-scale process that provides the cohesive strength of the soil at the InSight landing site is not known. Nonetheless, it is likely a combination of interparticle bonding by cementation, electrostatic attraction due to surface tension, and interlocking of the particles. In particular, a broad particle size distribution allows particles to interlock, providing mechanical bonds to create a supporting network which retains large pore spaces. Moreover, it was found in laboratory studies that low environmental pressure or hard vacuum result in a significant increase in cohesion of sands (Bromwell, 1966), which may help to explain the high cohesion apparent in the InSight images. Nevertheless, if soil cohesion is closer to the upper limit of 14 kPa (Marteau et al., 2021), these mechanisms may not be sufficient and particle cementation may be required to provide the necessary bonding.

In the light of the above discussion, grain size estimates based on a comparison with laboratory experiments of essentially cohesionless sand need to be interpreted with caution. Also, it has to be kept in mind that the derived grain sizes are representative of

the larger particles in the mixture, with 85 to 95% of particles being smaller. Therefore, a significant amount of smaller, dust sized particles could be present, increasing soil cohesion and potentially explaining the presence of steep walls and clods. As the influence of cohesion on thermal conductivity remains poorly constrained, estimates of particle size remain uncertain. However, it seems likely that 85 to 95% of all particles are smaller than 104-173 μm based on a comparison with laboratory experiments (Presley & Christensen, 1997) and the fact that the investigated soil appears to be an eolian deposit (Grant et al., 2020; Weitz et al., 2020).

Average soil thermal conductivity in the 0.03 to 0.37 m depth range determined here is very similar to that derived from surface thermal inertia measurements using the HP^3 radiometer (Mueller et al., 2020). While a thin low conductivity layer of thickness below 4 mm is required to explain the surface temperature response to solar eclipses by the martian moon Phobos (Mueller et al., 2021), diurnal surface temperatures sensitive to the upper ∼0.04-0.08 m of the soil are consistent with a thermal conductivity of 0.041± 0.013 W m^{-1} K^{-1} (Piqueux et al., 2021). Therefore, the thermal data suggest that the soil is largely homogeneous to a depth of 0.37 m.

Soil densities compatible with the temperature data are 1210^{+219}_{-102} kg m^{-3} if soil properties in the 0.03 to 0.37 m depth range are assumed to be similar to those derived from surface thermal inertia measurements (Golombek, Warner, et al., 2020). This falls within the range of density estimates for other martian landing sites with crusty to cloddy soils, for which values between 1100 to 1600 kg m^{-3} have been reported (Golombek et al., 2008). Furthermore, the range of admissible densities determined here is compatible with pre-landing estimates of 1300 kg m^{-3} (Morgan et al., 2018). These estimates of soil density can be converted to an estimate of bulk porosity if the density of the constituent particles is assumed to be known. Here we assume particle density to be similar to that found for basaltic martian meteorites, which have densities of 3100 to 3400 kg m^{-3} (Coulson et al., 2007; Britt et al., 2012). Furthermore, petrological modeling indicates densities of 3100 kg m^{-3} (Baratoux et al., 2014), such that the median densities derived above would correspond to a bulk porosity of ∼61 %. While this may appear large, it is quite consistent with results obtained at the Phoenix landing site (55 %, Zent et al. (2010)) as well as the fact that mole hammering created a significant hole by compacting void spaces during the early phases of probe insertion.

519 Experimental results on thermal conductivity as a function of porosity for various
520 extra-terrestrial soil simulants under terrestrial atmospheric conditions are summarized
521 by Becker & Vrettos (2016). Of the materials tested, three sands show grain-size char-
522 acteristics similar to the soil encountered at the InSight landing site. These poorly-graded
523 sands with mean grain sizes between 0.2 and 0.3 mm exhibit a thermal conductivity around
524 0.2 W m^{-1} K^{-1} at a typical porosity of 50%. In order to extrapolate conductivity to Mar-
525 tian atmospheric conditions we scale the gas contribution to the conductivity to 20-25%
526 of the terrestrial value as suggested by the results of Huetter et al. (2008). Adopting the
527 analytical model by Haigh (2012) for the extrapolation, we obtain a proportional reduc-
528 tion of the terrestrial conductivity value, resulting in predicted thermal conductivities
529 close to 0.04-0.05 W m^{-1} K^{-1} under martian atmopsheric conditions. This indicates that
530 high porosities are compatible with the thermal properties determined above.

531 If radiometrically derived surface thermal inertia is not used as an additional con-
532 straint, soil density estimates are reduced to 1007^{+176}_{-74} kg m^{-3}, and resulting porosity
533 estimates would increase to 68 %. However, there are no strong indications of changing
534 soil parameters in the depth range investigated here (Golombek, Warner, et al., 2020),
535 and the constantly slow progress of the mole also argues for a rather homogeneous soil
536 column. Therefore, the larger density estimates of 1211^{+149}_{-113} kg m^{-1} kg m^{-3} appear to
537 be more appropriate. Note, however, that it has been argued that a transition to cohe-
538 sionless sand may be present at a depth of 0.2 m (Hudson et al., 2020), but this is dif-
539 ficult to reconcile with the apparent similarity of thermal properties derived from radio-
540 metric measurements (Piqueux et al., 2021) and the results presented here.

541 The thermal conductivity measured here falls within the range of predictions used
542 for designing the HP^3 instrument (Grott et al., 2007; Spohn et al., 2018), which was 0.02
543 to 0.1 W m^{-1} K^{-1}. Based on the measurement of soil thermal conductivity at the In-
544 Sight landing site and assuming heat flow to be 19 to 24 mW m^{-2} (Plesa, Grott, Tosi,
545 et al., 2016), the subsurface thermal gradient is expected to be 0.45 to 0.64 K m^{-1}. This
546 is well above the design limit of 0.2 K m^{-1} to guarantee an overall 1-σ heat flow uncer-
547 tainty of 2.2 mW m^{-2} (Spohn et al., 2018). The relatively low thermal conductivity of
548 0.039 ± 0.002 W m^{-1} K^{-1} further reduces the influence of perturbations to the subsur-
549 face heat flow, which can be caused by, e.g., the InSight lander (Grott, 2009; Siegler et
550 al., 2017), interannual variations of surface temperature (Grott et al., 2007), as well as
551 surface temperature changes induced by martian dust storms (Plesa, Grott, Lemmon,

et al., 2016). The thermal conductivity determined here will therefore help to design future heat flow probes by providing important constraints on the thermophysical properties of the martian soil.

Soil thermal conductivities derived here and those derived from radiometric measurements of surface brightness temperatures (Piqueux et al., 2021) place strong constraints on the allowable degree of soil cementation. However, these results are difficult to reconcile with the analysis of image data, which strongly suggests an indurated duricrust to be present (Golombek, Warner, et al., 2020), as well as the analysis of soil mechanical properties, which argues for soil cohesion in the 2 to 14 kPa range (Marteau et al., 2021). When compared to other martian landing sites, thermal properties are thus similar to those of crusty to cloddy soils (thermal inertia of 200 to 326 J m^{-2} K^{-1} $s^{-1/2}$, cohesion of 0 to 4 kPa), while mechanical properties are more consistent with blocky to indurated soils (thermal inertia of 368 to 410 J m^{-2} K^{-1} $s^{-1/2}$, cohesion of 3 to 11 kPa, Golombek et al. (2008)). This apparent discrepancy between the interpretation of the thermal and mechanical properties cannot be resolved here and certainly deserves further study.

Acknowledgments

The design, building of and research into the HP^3 has been supported by the German Aerospace Center DLR, by NASA, the AW, and the Polish Academy of Science. The numerical code and data necessary to reproduce the results of this paper have been made publicly available in Grott (2021). Part of this work was performed at the Jet Propulsion Laboratory, California Institute of Technology, under a contract with NASA. US government support is gratefully acknowledged. This paper is InSight Contribution Number 210.

References

Banerdt, W. B., Smrekar, S. E., Banfield, D., Giardini, D., Golombek, M., Johnson, C. L., ... Wieczorek, M. (2020). Initial results from the InSight mission on Mars. *Nature Geoscience*, *13*(3), 183-189. doi: 10.1038/s41561-020-0544-y

Banin, A., Clark, B. C., & Waenke, H. (1992). Surface chemistry and mineralogy. In M. George (Ed.), *Mars* (p. 594-625).

Baratoux, D., Samuel, H., Michaut, C., Toplis, M. J., Monnereau, M., Wieczorek,

M., ... Kurita, K. (2014). Petrological constraints on the density of the Martian crust. *Journal of Geophysical Research (Planets)*, *119*(7), 1707-1727. doi: 10.1002/2014JE004642

Becker, A., & Vrettos, C. (2016). Tests on the thermal conductivity of regolith quasi-analogues at different porosities. In *Earth and space 2016* (p. 9-15). doi: 10.1061/9780784479971.002

Britt, D. T., Macke, R. J., Kiefer, W. S., Irving, A. J., Hupé, G., & Consolmagno, G. J. (2012). The Density, Porosity, and Magnetic Susceptibility of Two Recent Meteorite Falls: Tissint and Sutter's Mill. *Meteoritics and Planetary Science Supplement*, *75*, 5350.

Bromwell, L. G. (1966). *The friction of quartz in high vacuum* (Tech. Rep. No. 3-101). Department of Civil Engineering, M.I.T. Cambridge, MA: Research In Earth Physics, Phase Report No. 7.

Christensen, P. R., & Moore, H. J. (1992). The martian surface layer. In M. George (Ed.), *Mars* (p. 686-729).

Coulson, I. M., Beech, M., & Nie, W. (2007). Physical properties of Martian meteorites: Porosity and density measurements. *Meteoritics and Planetary Science*, *42*(12), 2043-2054. doi: 10.1111/j.1945-5100.2007.tb01006.x

Ditteon, R. (1982). Daily temperature variations on Mars. *Journal of Geophysical Research*, *87*, 10197-10214. doi: 10.1029/JB087iB12p10197

Edgett, K. S., Yingst, R. A., Minitti, M. E., Goetz, W., Kah, L. C., Kennedy, M. R., ... MSL Science Team (2013, March). Mars Hand Lens Imager (MAHLI) Efforts and Observations at the "Rocknest" Eolian Sand Shadow in Curiosity's Gale Crater Field Site. In *Lunar and planetary science conference* (p. 1201).

Edwards, C. S., Piqueux, S., Hamilton, V. E., Fergason, R. L., Herkenhoff, K. E., Vasavada, A. R., ... Smith, M. D. (2018). The Thermophysical Properties of the Bagnold Dunes, Mars: Ground-Truthing Orbital Data. *Journal of Geophysical Research (Planets)*, *123*(5), 1307-1326. doi: 10.1029/2017JE005501

Fergason, R., Christensen, P., Bell, J., Golombek, M., Herkenhoff, K., & Kieffer, H. (2006). Physical properties of the Mars Exploration Rover landing sites as inferred from Mini-TES-derived thermal inertia. *Journal of Geophysical Research (Planets)*, *111*(E2), E02S21. doi: 10.1029/2005JE002583

Golombek, M., Grott, M., Kargl, G., Andrade, J., Marshall, J., Warner, N., ...

Banerdt, W. B. (2018). Geology and Physical Properties Investigations by the InSight Lander. *Space Science Reviews*, *214*(5), 84. doi: 10.1007/s11214-018-0512-7

Golombek, M., Haldemann, A. F. C., Simpson, R. A., Fergason, R. L., Putzig, N. E., Arvidson, R. E., ... Mellon, M. T. (2008). Martian surface properties from joint analysis of orbital, Earth-based, and surface observations. In I. Bell Jim (Ed.), *The martian surface - composition, mineralogy, and physical properties* (p. 468).

Golombek, M., Kass, D., Williams, N., Warner, N., Daubar, I., Piqueux, S., ... Pike, W. T. (2020). Assessment of InSight Landing Site Predictions. *Journal of Geophysical Research (Planets)*, *125*(8), e06502. doi: 10.1029/2020JE006502

Golombek, M., Kipp, D., Warner, N., Daubar, I. J., Fergason, R., Kirk, R. L., ... Banerdt, W. B. (2017). Selection of the InSight Landing Site. *Space Science Reviews*, *211*(1-4), 5-95. doi: 10.1007/s11214-016-0321-9

Golombek, M., Warner, N. H., Grant, J. A., Hauber, E., Ansan, V., Weitz, C. M., ... Banerdt, W. B. (2020). Geology of the InSight landing site on Mars. *Nature Communications*, *11*, 1014. doi: 10.1038/s41467-020-14679-1

Golombek, M., Williams, N., Warner, N. H., Parker, T., Williams, M. G., Daubar, I., ... Sklyanskiy, E. (2020). Location and Setting of the Mars InSight Lander, Instruments, and Landing Site. *Earth and Space Science*, *7*(10), e01248. doi: 10.1029/2020EA001248

Gómez-Elvira, J., Armiens, C., Castañer, L., Domínguez, M., Genzer, M., Gómez, F., ... Martín-Torres, J. (2012). REMS: The Environmental Sensor Suite for the Mars Science Laboratory Rover. *Space Science Reviews*, *170*(1-4), 583-640. doi: 10.1007/s11214-012-9921-1

Grant, J. A., Warner, N. H., Weitz, C. M., Golombek, M. P., Wilson, S. A., Baker, M., ... Banks, M. E. (2020). Degradation of Homestead Hollow at the InSight Landing Site Based on the Distribution and Properties of Local Deposits. *Journal of Geophysical Research (Planets)*, *125*(4), e06350. doi: 10.1029/2019JE006350

Grott, M. (2009). Thermal disturbances caused by lander shadowing and the measurability of the martian planetary heat flow. *Planetary and Space Science*, *57*(1), 71-77. doi: 10.1016/j.pss.2008.11.005

Grott, M. (2021). Supplementary Material for "Thermal Conductivity of the Martian Regolith at the InSight Landing site from HP^3 Active Heating Experiments".

Figshare. doi: https://doi.org/10.6084/m9.figshare.c.5255468

Grott, M., Helbert, J., & Nadalini, R. (2007). Thermal structure of Martian soil and the measurability of the planetary heat flow. *Journal of Geophysical Research (Planets)*, *112*(E9), E09004. doi: 10.1029/2007JE002905

Grott, M., Knollenberg, J., & Krause, C. (2010). Apollo lunar heat flow experiment revisited: A critical reassessment of the in situ thermal conductivity determination. *Journal of Geophysical Research (Planets)*, *115*(E11), E11005. doi: 10.1029/2010JE003612

Grott, M., Spohn, T., Knollenberg, J., Krause, C., Scharringhausen, M., Wippermann, T., ... Banerdt, W. B. (2019). Calibration of the Heat Flow and Physical Properties Package (HP^3) for the InSight Mars Mission. *Earth and Space Science*, *6*(12), 2556-2574. doi: 10.1029/2019EA000670

GUM. (2008). *Evaluation of measurement data Guide to the expression of uncertainty in measurement*. Joint Committee for Guides in Metrology.

Haigh, S. (2012). Thermal conductivity of sands. *Gotechnique*, *62*(7), 617-625. doi: 10.1680/geot.11.P.043

Hamilton, V. E., Vasavada, A. R., Sebastián, E., Torre Juárez, M., Ramos, M., Armiens, C., ... Zorzano, M.-P. (2014). Observations and preliminary science results from the first 100 sols of MSL Rover Environmental Monitoring Station ground temperature sensor measurements at Gale Crater. *Journal of Geophysical Research (Planets)*, *119*(4), 745-770. doi: 10.1002/2013JE004520

Hammerschmidt, U., & Sabuga, W. (2000). Transient hot wire (THW) method: Uncertainty Assessment. *Intern. J. Thermophys.*, *21*(6), 1225-1278.

Haskin, L. A., Wang, A., Jolliff, B. L., McSween, H. Y., Clark, B. C., Des Marais, D. J., ... Soderblom, L. (2005). Water alteration of rocks and soils on Mars at the Spirit rover site in Gusev crater. *Nature*, *436*(7047), 66-69. doi: 10.1038/nature03640

Hecht, M. H., Kounaves, S. P., Quinn, R. C., West, S. J., Young, S. M. M., Ming, D. W., ... Smith, P. H. (2009). Detection of Perchlorate and the Soluble Chemistry of Martian Soil at the Phoenix Lander Site. *Science*, *325*(5936), 64. doi: 10.1126/science.1172466

Herkenhoff, K. E., Golombek, M. P., Guinness, E. A., Johnson, J. B., Kusack, A., Richter, L., ... Gorevan, S. (2008). In situ observations of the physical properties

of the Martian surface. In I. Bell Jim (Ed.), *The martian surface - composition, mineralogy, and physical properties* (p. 451).

Hudson, T. L., Deen, R., Marteau, E., Golombek, M., Hurst, K., Spohn, T., ... Knollenberg, J. (2020, March). InSight HP3 Mole Near-Surface Motion and Subsurface Implications. In *Lunar and planetary science conference* (p. 1217).

Huetter, E. S., Koemle, N. I., Kargl, G., & Kaufmann, E. (2008, December). Determination of the effective thermal conductivity of granular materials under varying pressure conditions. *Journal of Geophysical Research (Planets)*, *113*(E12), E12004. doi: 10.1029/2008JE003085

Hurowitz, J. A., McLennan, S. M., Tosca, N. J., Arvidson, R. E., Michalski, J. R., Ming, D. W., ... Squyres, S. W. (2006). In situ and experimental evidence for acidic weathering of rocks and soils on Mars. *Journal of Geophysical Research (Planets)*, *111*(E2), E02S19. doi: 10.1029/2005JE002515

Jaeger, J. C. (1956). Conduction of Heat in an Infinite Region Bounded Internally by a Circular Cylinder of a Perfect Conductor. *Australian Journal of Physics*, *9*, 167. doi: 10.1071/PH560167

Jakosky, B. M., & Christensen, P. R. (1986). Are the Viking Lander sites representative of the surface of Mars? *Icaurs*, *66*(1), 125-133. doi: 10.1016/0019-1035(86)90012-6

Kieffer, H. H., Martin, T. Z., Peterfreund, A. R., Jakosky, B. M., Miner, E. D., & Palluconi, F. D. (1977). Thermal and albedo mapping of Mars during the Viking primary mission. *Journal of Geophysical Research*, *82*(B28), 4249-4292. doi: 10.1029/JS082i028p04249

Kok, J. F., Parteli, E. J. R., Michaels, T. I., & Karam, D. B. (2012). The physics of wind-blown sand and dust. *Reports on Progress in Physics*, *75*(10), 106901. doi: 10.1088/0034-4885/75/10/106901

Kounaves, S. P., Chaniotakis, N. A., Chevrier, V. F., Carrier, B. L., Folds, K. E., Hansen, V. M., ... Weber, A. W. (2014). Identification of the perchlorate parent salts at the Phoenix Mars landing site and possible implications. *Icarus*, *232*, 226-231. doi: 10.1016/j.icarus.2014.01.016

Maki, J. N., Golombek, M., Deen, R., Abarca, H., Sorice, C., Goodsall, T., ... Banerdt, W. B. (2018, September). The Color Cameras on the InSight Lander. *Space Science Reviews*, *214*(6), 105. doi: 10.1007/s11214-018-0536-z

Marshall, J. P., Hudson, T. L., & Andrade, J. E. (2017). Experimental Investigation of InSight HP^3 Mole Interaction with Martian Regolith Simulant. Quasi-Static and Dynamic Penetration Testing. *Space Science Reviews*, *211*(1-4), 239-258. doi: 10.1007/s11214-016-0329-1

Marteau, E., Golombek, M., Vrettos, C., & Garvin, J. (2021). Soil Mechanical Properties at the InSight Landing Site on Mars. In *Lunar and planetary science conference* (p. 2067).

Martinez, Alejandro, Huang, Lin, & Gomez, Michael G. (2020). Enhancement of the thermal conductivity of sands via microbially-induced calcite precipitation. *E3S Web Conf.*, *205*, 09011. doi: 10.1051/e3sconf/202020509011

Mellon, M. T., Arvidson, R. E., Sizemore, H. G., Searls, M. L., Blaney, D. L., Cull, S., ... Zent, A. P. (2009). Ground ice at the phoenix landing site: Stability state and origin. *Journal of Geophysical Research: Planets*, *114*(E1). doi: https://doi.org/10.1029/2009JE003417

Mellon, M. T., Jakosky, B. M., Kieffer, H. H., & Christensen, P. R. (2000). High-Resolution Thermal Inertia Mapping from the Mars Global Surveyor Thermal Emission Spectrometer. *Icaurs*, *148*(2), 437-455. doi: 10.1006/icar.2000.6503

Moore, H. J., Bickler, D. B., Crisp, J. A., Eisen, H. J., Gensler, J. A., Haldemann, A. F. C., ... Pavlics, F. (1999). Soil-like deposits observed by Sojourner, the Pathfinder rover. *Journal of Geophysical Research*, *104*(E4), 8729-8746. doi: 10.1029/1998JE900005

Morgan, P., Grott, M., Knapmeyer-Endrun, B., Golombek, M., Delage, P., Lognonné, P., ... Kedar, S. (2018). A Pre-Landing Assessment of Regolith Properties at the InSight Landing Site. *Space Science Reviews*, *214*(6), 104. doi: 10.1007/s11214-018-0537-y

Mueller, N. T., Knollenberg, J., Grott, M., Kopp, E., Walter, I., Krause, C., ... Smrekar, S. (2020). Calibration of the HP^3 Radiometer on InSight. *Earth and Space Science*, *7*(5), e01086. doi: 10.1029/2020EA001086

Mueller, N. T., Piqueux, S., Lemmon, M., Maki, J., Lorenz, R., Grott, M., ... Banerdt, W. (2021). Near surface properties derived from Phobos transits with HP^3 RAD on InSight, Mars. *Geophysical Research Letters*, *submitted*.

Mutch, T. A., Arvidson, R. E., Binder, A. B., Guinness, E. A., & Morris, E. C. (1977). The geology of the Viking lander 2 site. *Journal of Geophysical Research*,

748 *82*(B28), 4452-4467. doi: 10.1029/JS082i028p04452

749 Neugebauer, G., Münch, G., Kieffer, H., Chase, J., S. C., & Miner, E. (1971).
750 Mariner 1969 Infrared Radiometer Results: Temperatures and Thermal Properties
751 of the Martian Surface. *Astronomical Journal*, *76*, 719. doi: 10.1086/111189

752 Palluconi, F. D., & Kieffer, H. H. (1981). Thermal inertia mapping of Mars from 60S
753 to 60N. *Icarus*, *45*(2), 415-426. doi: 10.1016/0019-1035(81)90044-0

754 Piqueux, S., & Christensen, P. R. (2009a). A model of thermal conductivity for
755 planetary soils: 1. Theory for unconsolidated soils. *Journal of Geophysical Re-*
756 *search (Planets)*, *114*(E9), E09005. doi: 10.1029/2008JE003308

757 Piqueux, S., & Christensen, P. R. (2009b). A model of thermal conductivity for
758 planetary soils: 2. Theory for cemented soils. *Journal of Geophysical Research*
759 *(Planets)*, *114*(E9), E09006. doi: 10.1029/2008JE003309

760 Piqueux, S., Mueller, N., Grott, M., Siegler, M., Millour, E., Forget, F., ... Smrekar,
761 W., S.E. Banerdt (2021). Regolith Properties near the InSight Lander Derived
762 from 50 Sols of Radiometer Measurements. *Journal of Geophysical Research*
763 *(Planets)*, *submitted*.

764 Plesa, A. C., Grott, M., Lemmon, M. T., Müller, N., Piqueux, S., Siegler, M. A., ...
765 Spohn, T. (2016). Interannual perturbations of the Martian surface heat flow by
766 atmospheric dust opacity variations. *Journal of Geophysical Research (Planets)*,
767 *121*(10), 2166-2175. doi: 10.1002/2016JE005127

768 Plesa, A. C., Grott, M., Tosi, N., Breuer, D., Spohn, T., & Wieczorek, M. A.
769 (2016). How large are present-day heat flux variations across the surface of
770 Mars? *Journal of Geophysical Research (Planets)*, *121*(12), 2386-2403. doi:
771 10.1002/2016JE005126

772 Pollack, J. B., Colburn, D. S., Flasar, F. M., Kahn, R., Carlston, C. E., & Pi-
773 dek, D. G. (1979). Properties and effects of dust particles suspended in the
774 Martian atmosphere. *Journal of Geophysical Research*, *84*, 2929-2945. doi:
775 10.1029/JB084iB06p02929

776 Presley, M. A., & Christensen, P. R. (1997). The effect of bulk density and particle
777 size sorting on the thermal conductivity of particulate materials under Martian
778 atmospheric pressures. *Journal of Geophysical Research (Planets)*, *102*(E4),
779 9221-9230. doi: 10.1029/97JE00271

780 Presley, M. A., & Craddock, R. A. (2006). Thermal conductivity measurements of

781 particulate materials: 3. Natural samples and mixtures of particle sizes. *Journal of*
782 *Geophysical Research (Planets)*, *111*(E9), E09013. doi: 10.1029/2006JE002706
783 Presley, M. A., Craddock, R. A., & Zolotova, N. (2009). The effect of salt crust on
784 the thermal conductivity of one sample of fluvial particulate materials under Mar-
785 tian atmospheric pressures. *Journal of Geophysical Research (Planets)*, *114*(E11),
786 E11007. doi: 10.1029/2009JE003355
787 Putzig, N. E., & Mellon, M. T. (2007). Apparent thermal inertia and the surface
788 heterogeneity of Mars. *Icarus*, *191*(1), 68-94. doi: 10.1016/j.icarus.2007.05.013
789 Shaw, A., Arvidson, R. E., Bonitz, R., Carsten, J., Keller, H. U., Lemmon, M. T.,
790 ... Trebi-Ollennu, A. (2009). Phoenix soil physical properties investigation.
791 *Journal of Geophysical Research: Planets*, *114*(E1). doi: https://doi.org/10.1029/
792 2009JE003455
793 Siegler, M. A., Smrekar, S. E., Grott, M., Piqueux, S., Mueller, N., Williams, J.-P.,
794 ... Spohn, T. (2017, October). The InSight Mars Lander and Its Effect on the
795 Subsurface Thermal Environment. *Space Science Reviews*, *211*(1-4), 259-275. doi:
796 10.1007/s11214-017-0331-2
797 Spohn, T., Grott, M., Smrekar, S. E., Knollenberg, J., Hudson, T. L., Krause, C.,
798 ... Banerdt, W. B. (2018). The Heat Flow and Physical Properties Pack-
799 age (HP^3) for the InSight Mission. *Space Science Reviews*, *214*(5), 96. doi:
800 10.1007/s11214-018-0531-4
801 VIM. (2004). *International vocabulary of basic and general terms in metrology.* Inter-
802 national Organization for Standardization.
803 Warner, N. H., Golombek, M. P., Sweeney, J., Fergason, R., Kirk, R., & Schwartz,
804 C. (2017). Near Surface Stratigraphy and Regolith Production in Southwest-
805 ern Elysium Planitia, Mars: Implications for Hesperian-Amazonian Terrains and
806 the InSight Lander Mission. *Space Science Reviews*, *211*(1-4), 147-190. doi:
807 10.1007/s11214-017-0352-x
808 Weitz, C. M., Grant, J. A., Golombek, M. P., Warner, N. H., Hauber, E., Ansan, V.,
809 ... Kopp, M. (2020). Comparison of InSight Homestead Hollow to Hollows at the
810 Spirit Landing Site. *Journal of Geophysical Research (Planets)*, *125*(7), e06435.
811 doi: 10.1029/2020JE006435
812 Yingst, R. A., Kah, L. C., Palucis, M., Williams, R. M. E., Garvin, J., Bridges,
813 J. C., ... Wiens, R. C. (2013). Characteristics of pebble- and cobble-sized clasts

along the Curiosity rover traverse from Bradbury Landing to Rocknest. *Journal of Geophysical Research (Planets)*, *118*(11), 2361-2380. doi: 10.1002/2013JE004435

Zent, A. P., Hecht, M. H., Cobos, D. R., Wood, S. E., Hudson, T. L., Milkovich, S. M., ... Mellon, M. T. (2010). Initial results from the thermal and electrical conductivity probe (TECP) on Phoenix. *Journal of Geophysical Research (Planets)*, *115*(2), E00E14. doi: 10.1029/2009JE003420

Figure 1.

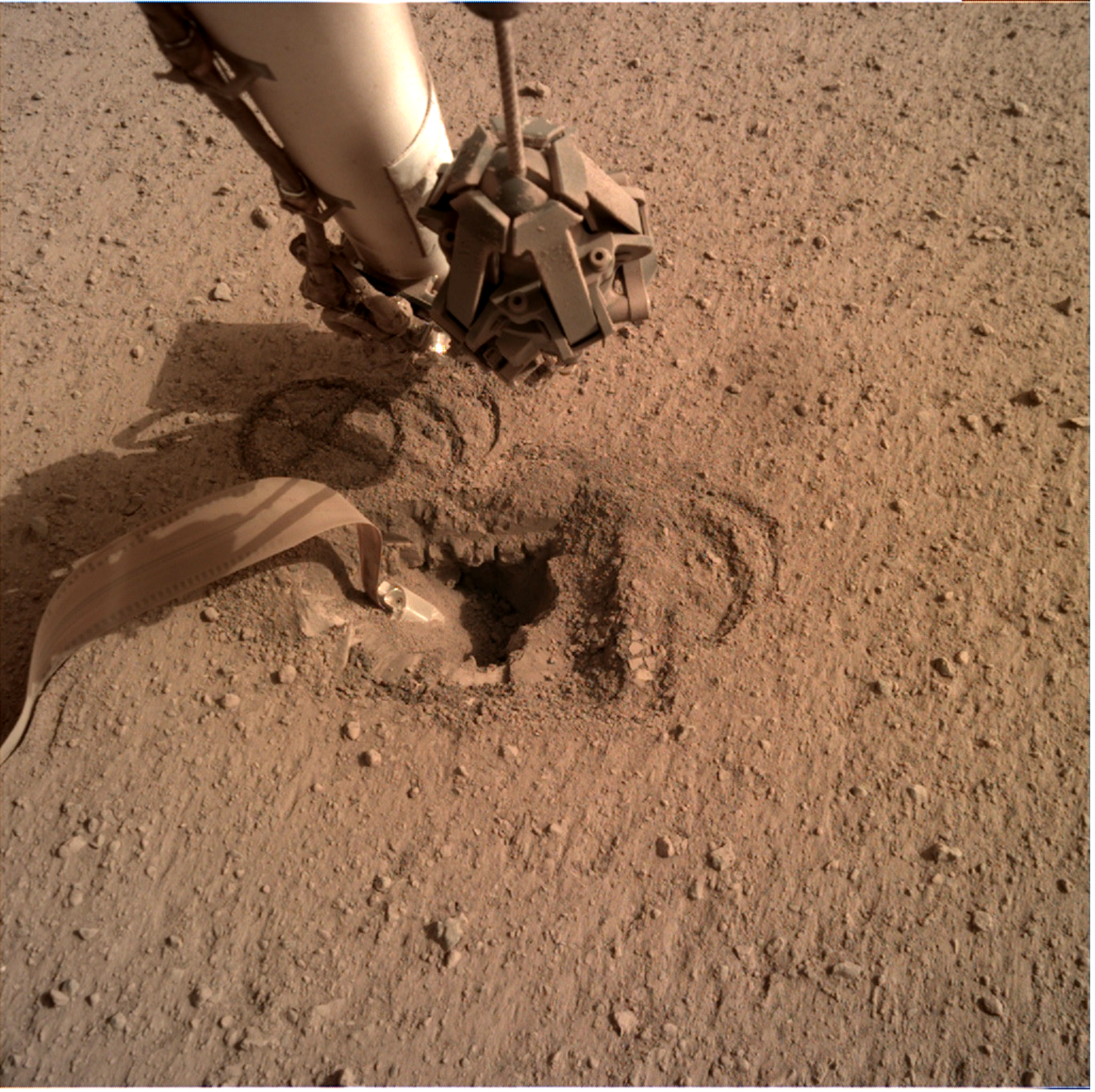

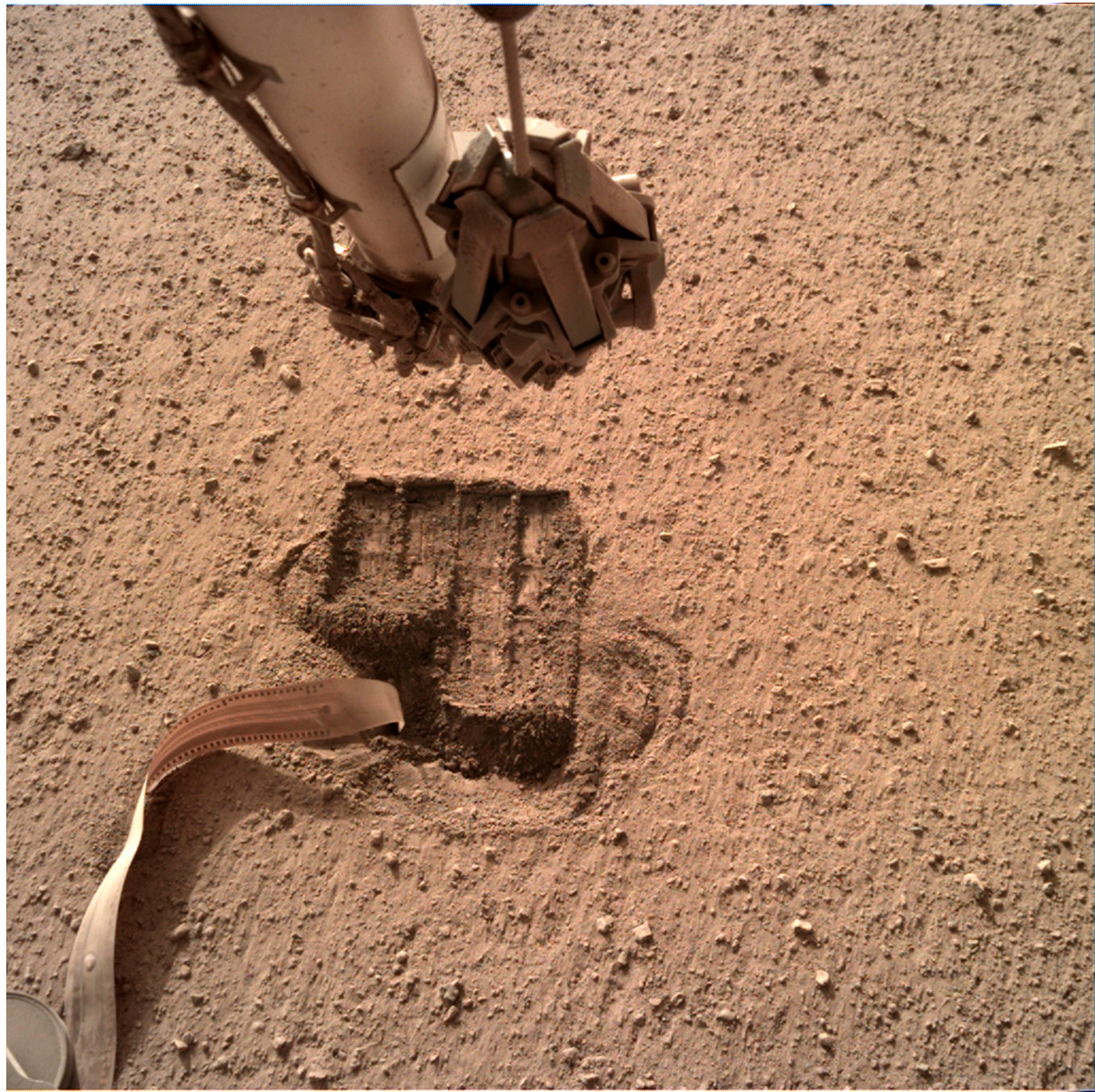

Figure 2.

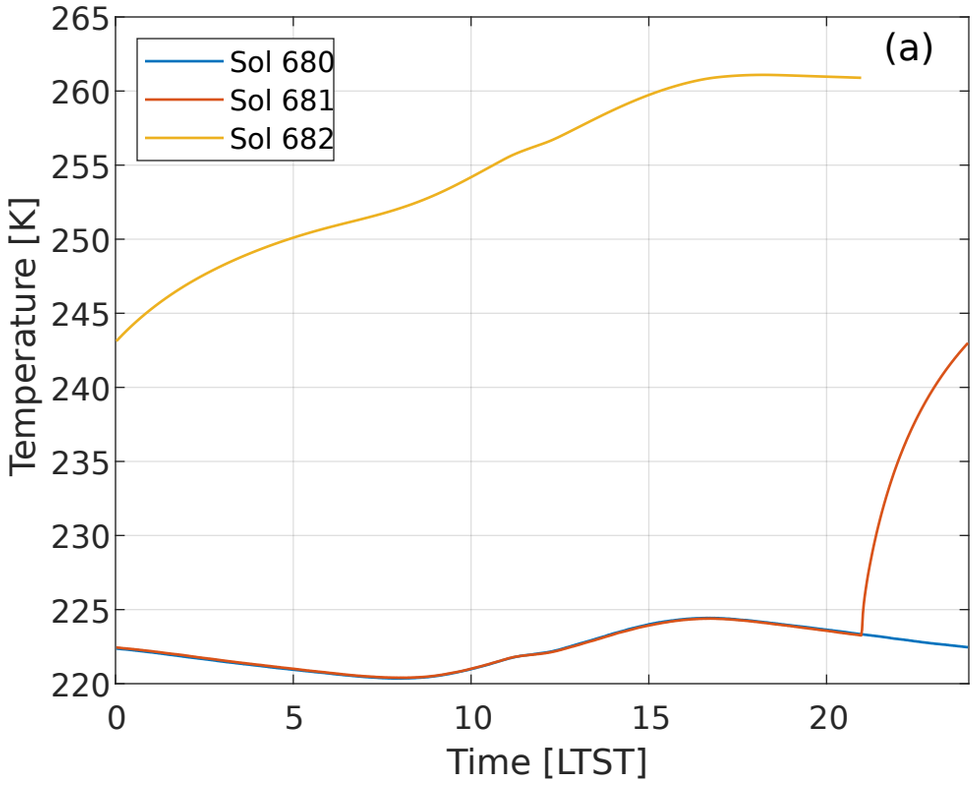
(a)
Sol 680
Sol 681
Sol 682
Temperature [K]
Time [LTST]

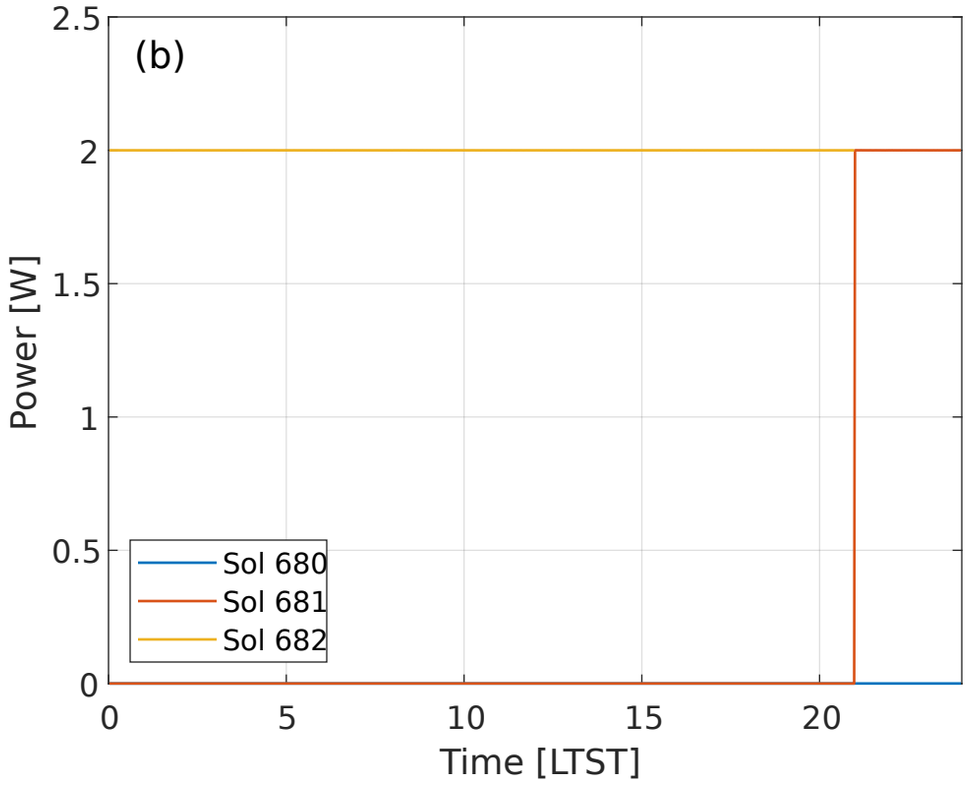
(b)
Sol 680
Sol 681
Sol 682
Power [W]
Time [LTST]

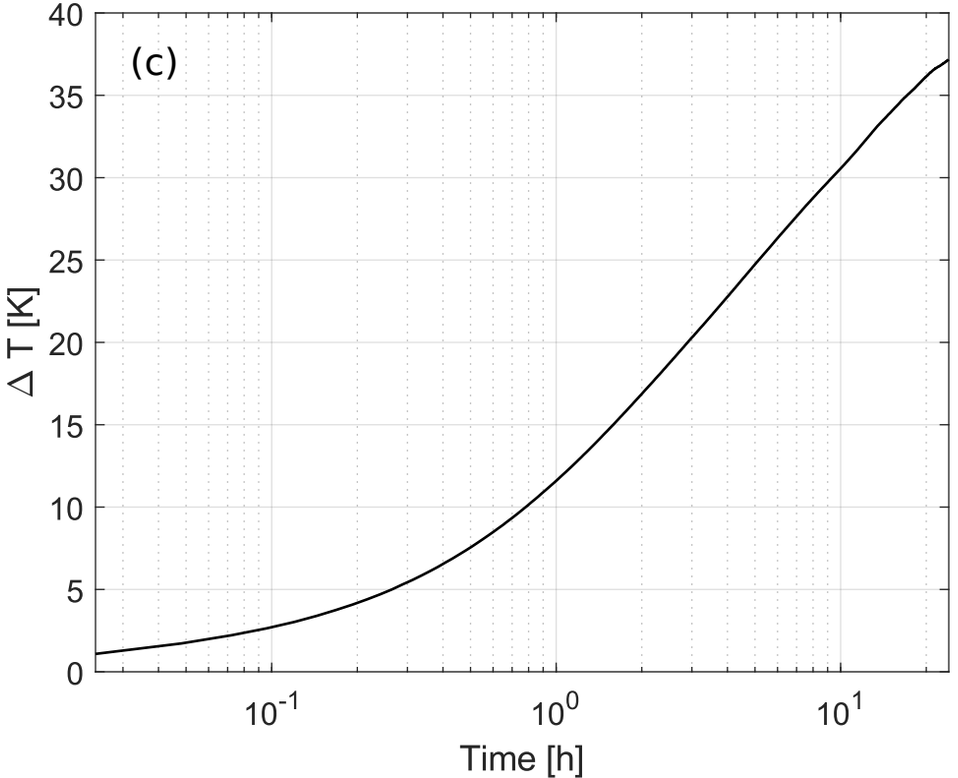
(c)
Δ T [K]
Time [h]

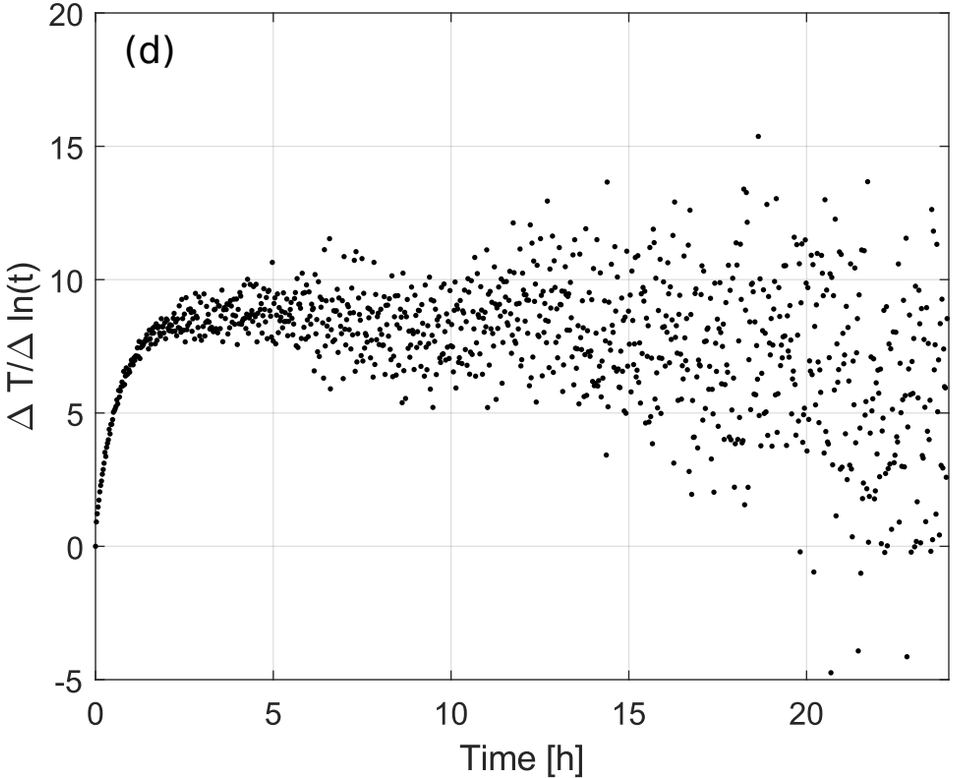
(d)
Δ T/Δ ln(t)
Time [h]

Figure 3.

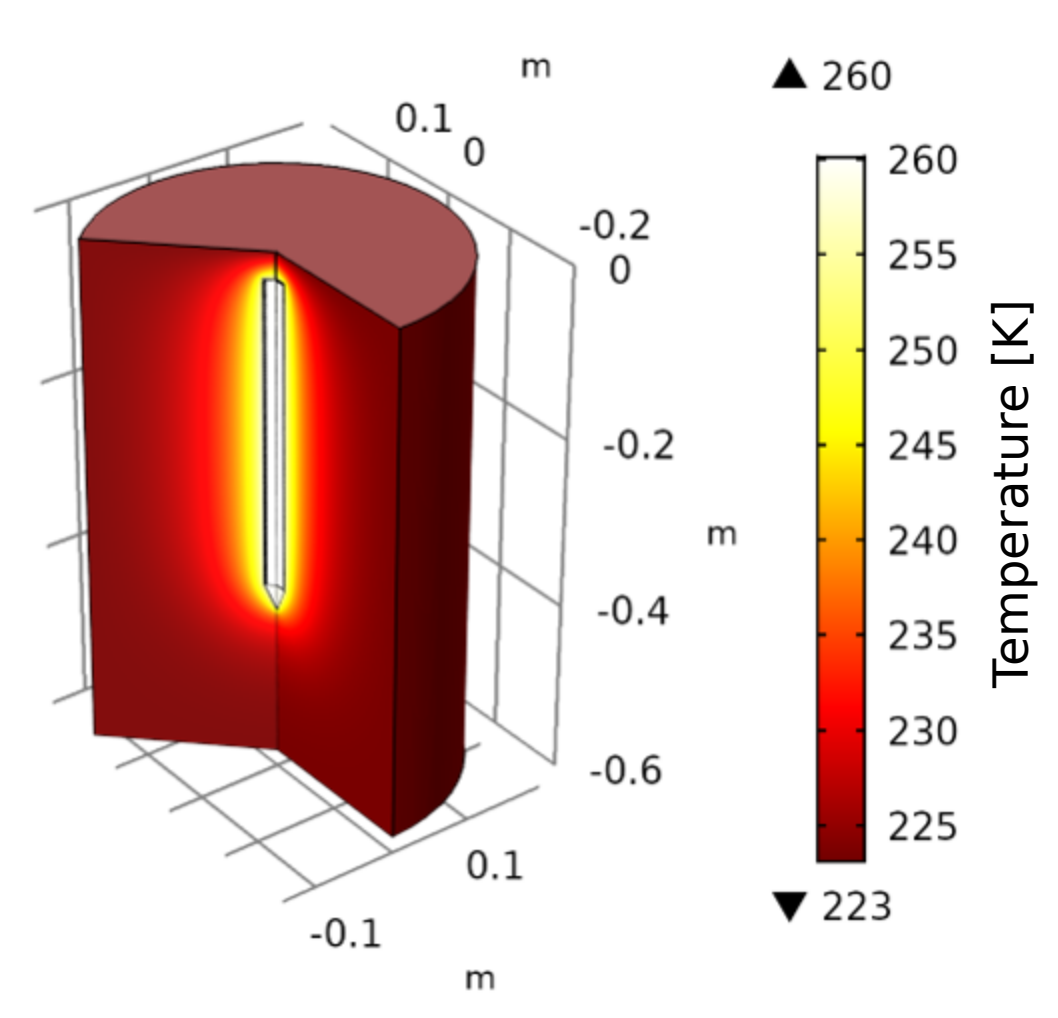
m
0.1
0
-0.2
0
-0.2
m
-0.4
-0.6
0.1
-0.1
m
▲ 260
260
255
250
245
240
235
230
225
▼ 223
Temperature [K]

Figure 4.

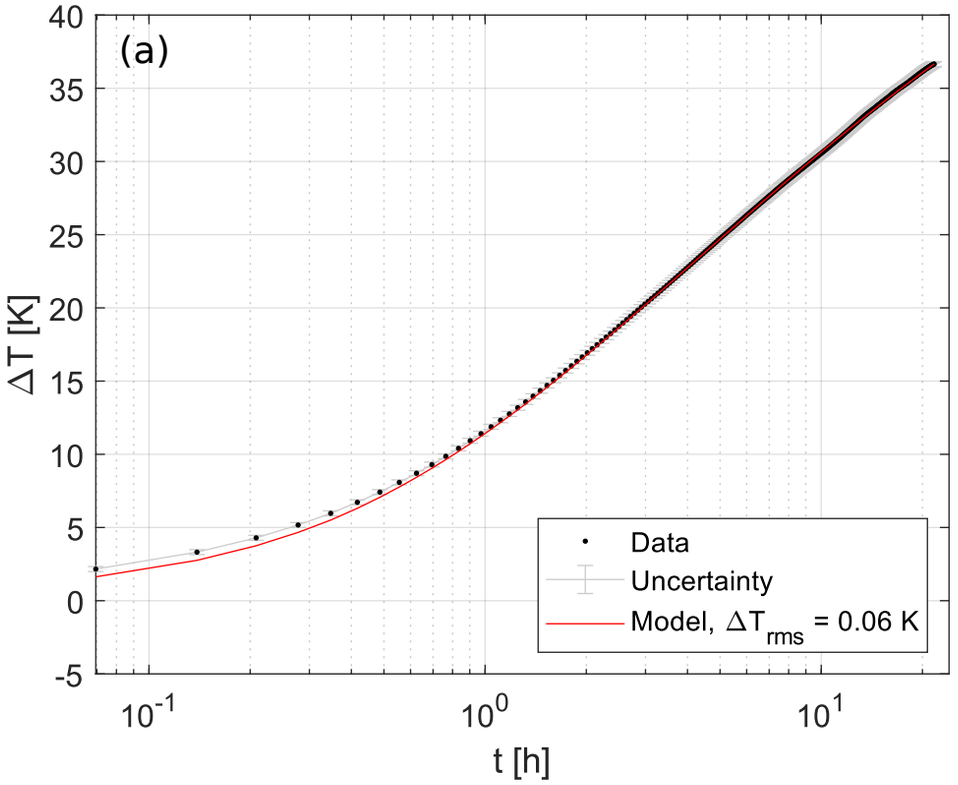
(a)
ΔT [K]
t [h]
Data
Uncertainty
Model, ΔT_rms = 0.06 K

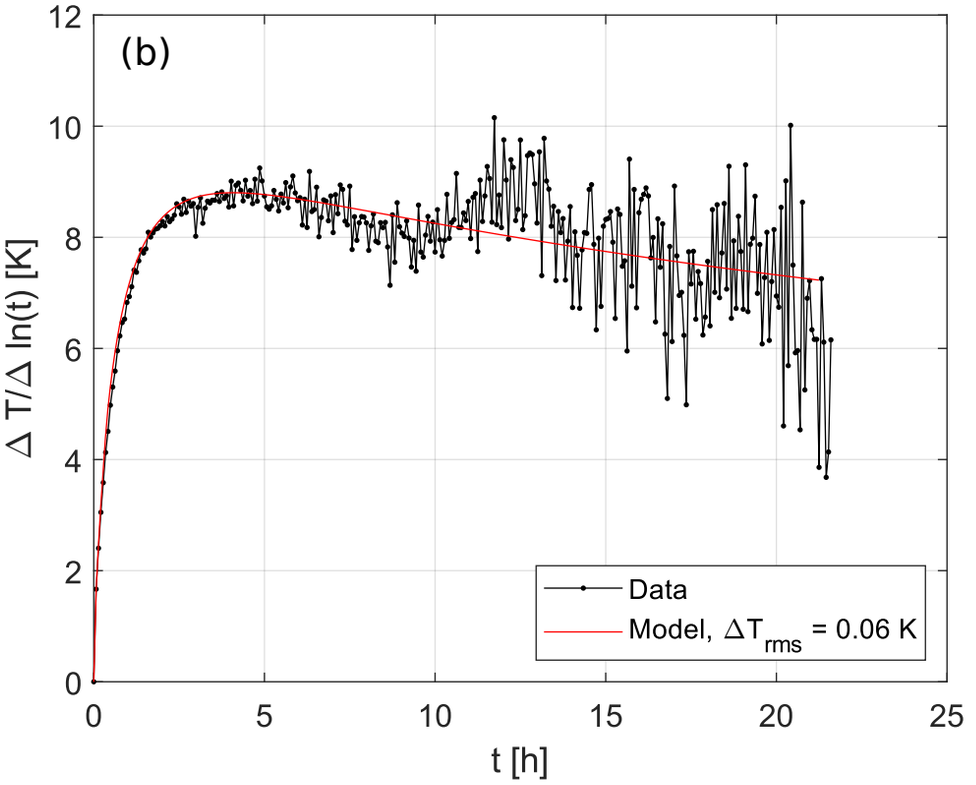
(b)
Δ T/Δ ln(t) [K]
t [h]
Data
Model, ΔT_rms = 0.06 K

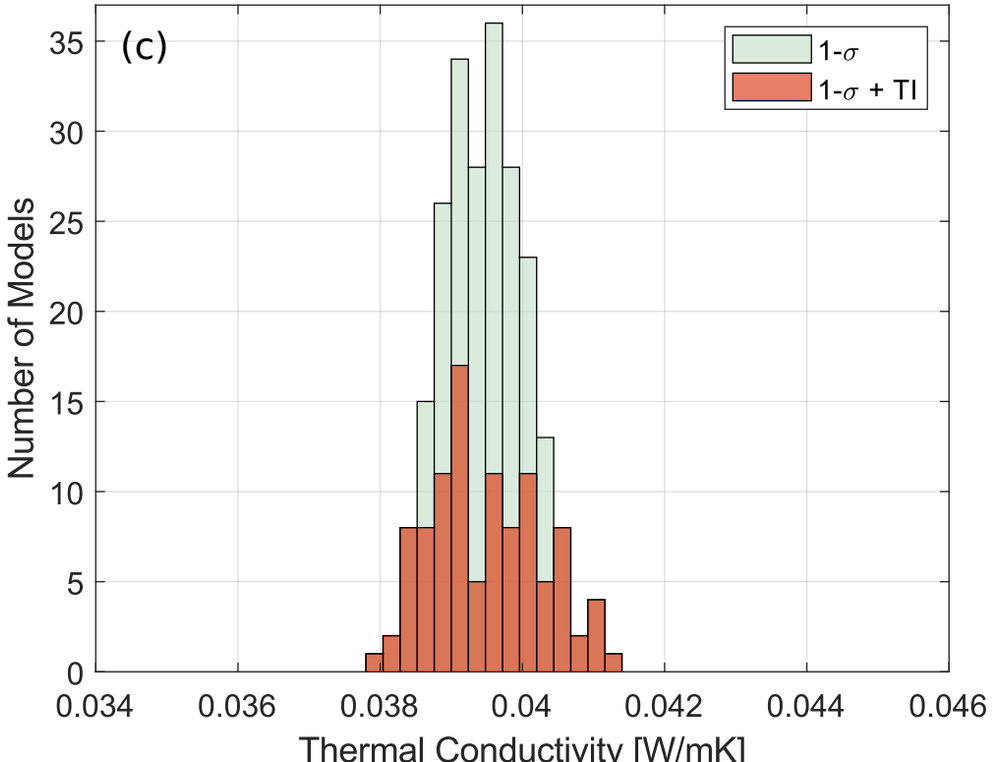
(c)
Number of Models
Thermal Conductivity [W/mK]
1-σ
1-σ + TI

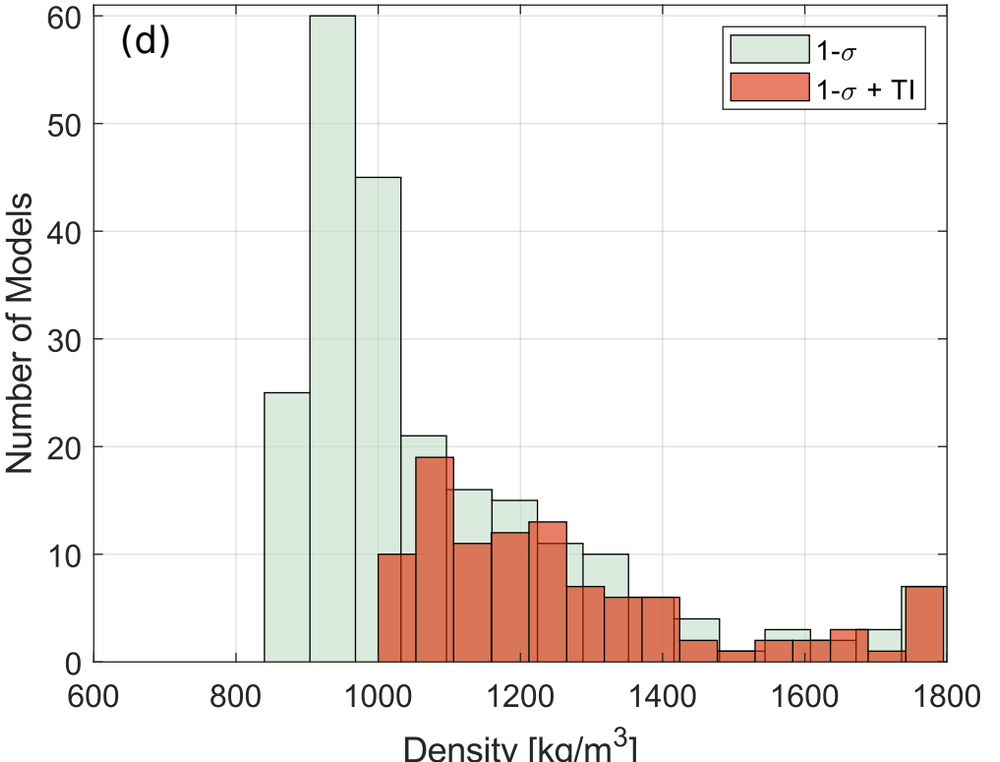
(d)
Number of Models
Density [kg/m3]
1-σ
1-σ + TI

Figure 5.

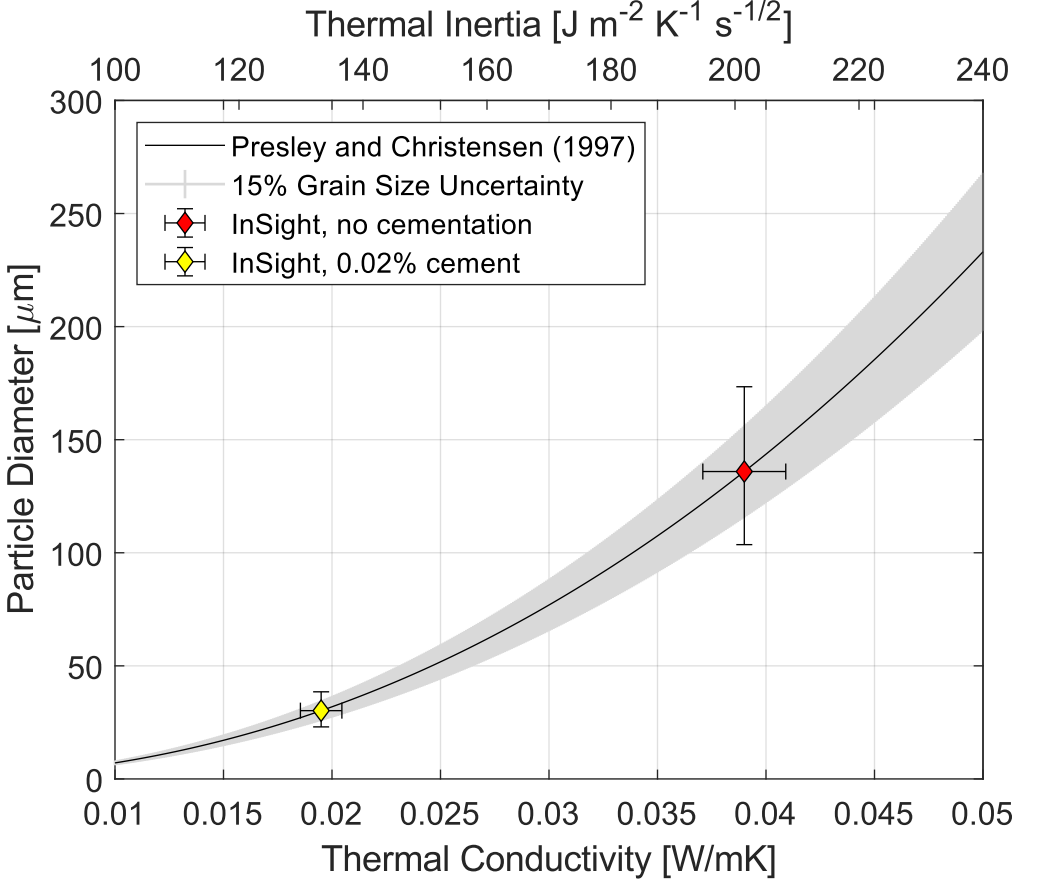
Thermal Inertia [J m^{-2} K^{-1} s$^{-1/2}$]
100
120
140
160
180
200
220
240
300
250
200
150
100
50
0
Particle Diameter [μm]
Presley and Christensen (1997)
15% Grain Size Uncertainty
InSight, no cementation
InSight, 0.02% cement
0.01
0.015
0.02
0.025
0.03
0.035
0.04
0.045
0.05
Thermal Conductivity [W/mK]